Spectral properties and geologic processes on Eros from combined NEAR NIS and MSI data sets

Noam R. IZENBERG,[1]* Scott L. MURCHIE,[1] James F. BELL, III,[2] Lucy A. McFADDEN,[3] Dennis D. WELLNITZ,[3] Beth E. CLARK,[4] and Michael J. GAFFEY[5]

[1]The Johns Hopkins University Applied Physics Laboratory, 11100 Johns Hopkins Road, Laurel, Maryland 20723, USA
[2]Cornell University, Center for Radiophysics and Space Research, Ithaca, New York 14853, USA
[3]University of Maryland, Astronomy Department, College Park, Maryland 20742, USA
[4]Ithaca College, Physics Department, Ithaca, New York 14850, USA
[5]University of North Dakota, Space Studies, Grand Forks, North Dakota 58202, USA
*Corresponding author. E-mail: noam.izenberg@jhuapl.edu

Abstract–From April 24 to May 14, 2000, the Near Earth Asteroid Rendezvous (NEAR) Shoemaker mission's near infrared spectrometer (NIS) obtained its highest resolution data of 433 Eros. High signal-to-noise ratio NIS reflectance spectra cover a wavelength range of 800–2400 nm, with footprint sizes from 213 × 427 m to 394 × 788 m. This paper describes improvement in instrument calibration by remediation of internally scattered light; derivation of a "pseudo channel" for NIS at 754 nm using Multispectral Imager (MSI) Eros approach maps at 951 and 754 nm; synthesis of a 3127-spectrum high-resolution data set with the improved calibration and expanded wavelength coverage; and investigation of global and localized spectral variation with respect to mineralogy, composition, and space weathering of Eros, comparing the findings with previous analyses. Scattered light removal reduces the "red" slope of Eros spectra, though not to the level seen by telescopic observations. The pseudo channel completes sampling of Eros' 1 micron (Band I) absorption feature, enabling direct comparison of NIS data with other asteroid and meteorite spectra without additional scaling or correction. Following scattered light removal and wavelength range extension, the spectral parameters of average Eros plot well inside the S(IV) field of Gaffey et al. (1993) and are consistent with the L6 chondrite meteorite fields of Gaffey and Gilbert (1998). Although Eros shows no evidence of mineralogical heterogeneity, modest spectral variations correlate with morphologically and geographically distinct areas of the asteroid. Eros bright-to-dark spectral ratios are largely consistent with laboratory "space weathering" experiment results and modeling of space weathering effects. Eros brightness variation unaccompanied by significant spectral variation departs from "lunar-type"—where band depths, slopes, and albedos all correlate—and "Ida-type"—where significant spectral variation is unaccompanied by corresponding brightness variation. The brightest areas on Eros—steep crater walls—have lesser spectral slope and deeper Band I, consistent with exposure of "fresher," less space weathered materials. Bright crater slope materials have opx/(opx + olv) of 0.24–0.29 and may be more representative of the subsurface mineralogy than "average" Eros, which is probably affected by space weathering. The floors of the large craters Psyche and Himeros have lower albedo and contain the most degraded or altered looking materials. NIS spectra retain a "red" spectral slope at greater than 2 microns. The recalibrated and expanded NIS spectra show better agreements with mixing models based on space weathering of chondritic mixtures.

INTRODUCTION

The near infrared spectrometer (NIS) instrument of the Near Earth Asteroid Rendezvous (NEAR) Shoemaker spacecraft measured reflected sunlight in the 800–2400 nm wavelength range. NIS science goals include mapping the composition and distribution of minerals on the surface of asteroid 433 Eros at spatial resolutions as high as a few hundred meters and providing information on the physical and textural properties of Eros' surface materials. NIS data complement high-resolution images from the Multispectral Imager (MSI) and low spatial resolution elemental

distribution from the X-ray and gamma ray spectrometers (XGRS) for identification of the materials composing Eros' surface (Veverka et al. 1997; Trombka et al. 2000; McCoy et al. 2001).

NIS is a grating spectrometer with 64 channels across 2 separate detectors. A Germanium (Ge) detector covers the short wavelengths of the instrument range (<1500 nm), and an Indium-Gallium-Arsenide (InGaAs) detector covers the longer wavelengths (Table 1 details the center wavelength and effective width of each NIS channel). The effective science range of NIS is ~800–2400 nm due to wavelength cutoffs and unacceptably low signal-to-noise at wavelengths longer than 2400 nm (Izenberg et al. 2000a). MSI has 7 color filters (plus 1 long bandpass "clear" filter). Filter 4, centered at 951 nm and 38 nm wide, corresponds closely to NIS channel 7, centered at 945.9 nm and 22 nm across (Murchie et al. 1999). Filter 3, centered at 754 nm and 19 nm wide is specifically

Table 1. NIS wavelengths.[a]

Channel #	Band center (nm)	Channel #	Band center (nm)
1	816.2	*33*	*1371.8*
2	837.8	*34*	*1414.9*
3	859.4	*35*	*1458.0*
4	881.0	*36*	*1501.1*
5	902.7	37	1544.2
6	924.3	38	1587.3
7	945.9	39	1630.4
8	967.5	40	1673.6
9	989.1	41	1716.7
10	1010.7	42	1759.8
11	1032.3	43	1802.9
12	1053.9	44	1846.0
13	1075.5	45	1889.1
14	1097.1	46	1932.2
15	1118.8	47	1975.3
16	1140.4	48	2018.4
17	1162.0	49	2061.5
18	1183.6	50	2104.7
19	1205.2	51	2147.8
20	1226.8	52	2190.9
21	1248.4	53	2234.0
22	1270.0	54	2277.1
23	1291.6	55	2320.2
24	1313.2	56	2363.3
25	1334.9	*57*	*2406.4*
26	1356.5	*58*	*2449.5*
27	1378.1	*59*	*2492.6*
28	1399.7	*60*	*2535.8*
29	1421.3	*61*	*2578.9*
30	1442.9	*62*	*2622.0*
31	1464.5	*63*	*2665.1*
32	1486.1	*64*	*2708.2*

[a]Germanium (Ge) detector channels are #s 1–32. Indium-Gallium-Arsenide (InGaAs) channels are #s 33–64. The channels in italics are low SNR or in cutoff and are not used for science. Ge channels are 22 nm across; InGaAs channels are 44 nm across.

chosen to sample the short-wavelength edge of the 1 micron (Band I) silicate absorption feature.

Initial results of the NIS investigation of Eros (Veverka et al. 2000; Bell et al. 2002) include large albedo variations but little color variation and little if any compositional variation. The largest observed spectral variations from low phase flyby (LPF) analysis (though still only a few percent) are in Band I depth. Band I is deeper in parts of the rims of Psyche, Himeros, and other large craters, and along Eros' equator. Initial mapping of the 2000 to 1000 nm band area ratio (BAR from Gaffey et al. [1993]) is consistent with at least the upper surface having a fairly uniform orthopyroxene to orthopyroxene + olivine (Cloutis et al. 1986) ratio of 0.3 to 0.4, with the possibility of a second high-calcium pyroxene present in the mineral mixture. MSI results include weak color variation yet strong reflectance variations on Eros, geological correlations for brightness features, and consistency of color variations with space weathering effects (Murchie et al. 2002a; Robinson et al. 2002). Observed brightness and spectral variations, though small, may indicate exposure of spectrally "fresher" materials by down-slope movement (Clark et al. 2001; Murchie et al. 2002a; Robinson et al. 2002). Fig. 1 shows an MSI reflectance map (951 nm) of the northern hemisphere of Eros with some of the major features such as craters, ridges, and Regio identified. These data, though low in spatial resolution relative to later orbital imaging, were acquired at the lowest phase angles observed by MSI (52°), just before orbit insertion, and had spatial resolutions comparable to the highest resolution NIS spectral data.

NIS and MSI observations of the earth, the moon, and Eros discussed in Izenberg et al. (2000a) and Murchie et al. (1999, 2002b) supplied initial cross-calibrations of the imager and spectrometer before orbital observations. In this paper, we improve the NIS calibration by remediating a significant contribution of scattered light within NIS, extend the effective spectrum of NIS by deriving a "pseudo" NIS channel at 754 nm based on MSI reflectance and color ratio data, and investigate global and localized spectral parameters with respect to the mineralogy and composition of Eros.

DATA CORRECTION AND REDUCTION

Scattered Light Removal

Initial NIS results show the spectrum of Eros appears substantially redder than in telescopic spectra (Murchie and Pieters 1996; Veverka et al. 2000; Clark et al. 2001; McFadden et al. 2001; Bell et al. 2002). Explanations for the red slope include combinations of "space weathering" effects and darkening/reddening mineral phases after Pieters et al. (2000) and Hapke (2001) and the possibility of a glassy component to surface materials (Bell et al. 2002). Explanations for the NIS mismatch with telescope data include errors in NIS calibration coefficients derived from on-
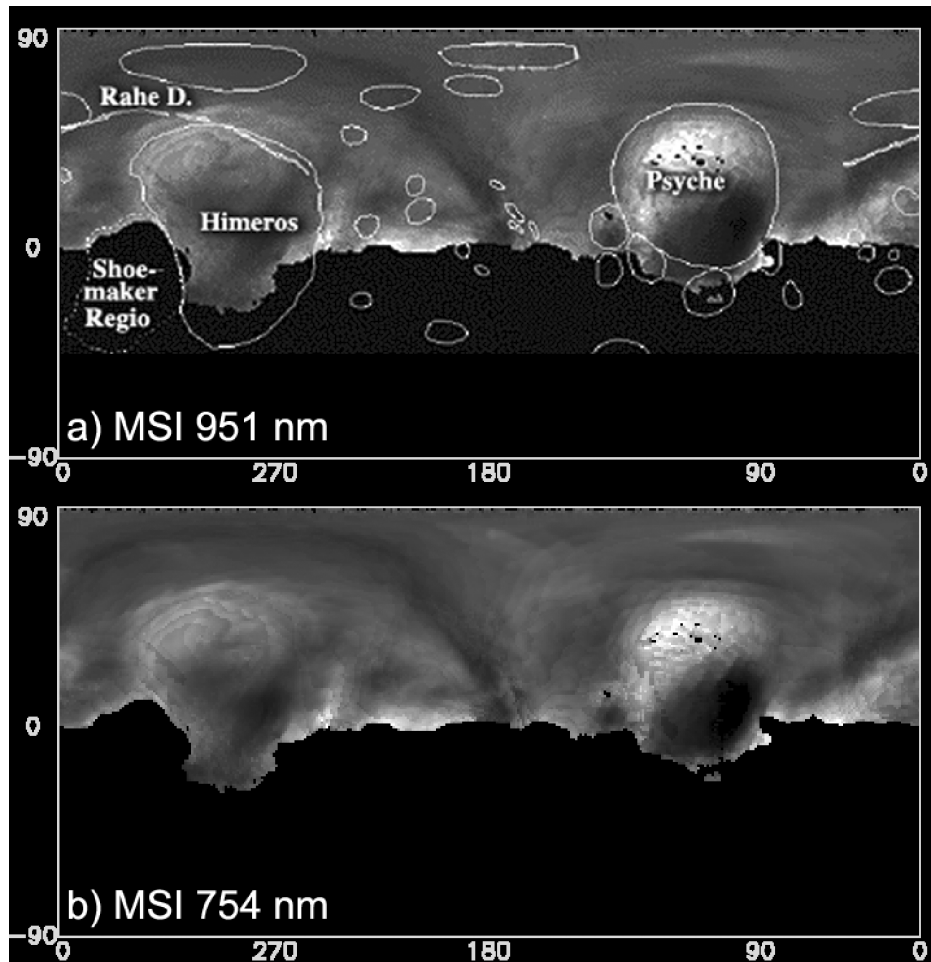
Fig. 1. Simple cylindrical projection maps of Eros with major surface features identified: a) resampled from MSI 951 nm approach images (filter 4), converted to reflectance, and photometrically corrected to an incidence angle of 30° and an emission angle of 0° (Murchie et al. 2002a). Mid-size craters are indicated with ellipses. (See Robinson et al. [2002] for more detailed nomenclature.) The floors of Psyche and Himeros are among the darkest materials on Eros. Wall and rim materials of Psyche and Himeros are some of the brightest; b) MSI 754 nm map, (filter 3) from Murchie et al. (2002a). The data are stretched the same as in Murchie et al. (2002a) but are presented here in grayscale.

ground radiometry (Izenberg et al. 2000a). Ground calibrations of the Comet Nucleus Tour's Contour Remote Imager and Spectrometer (CRISP) revealed an internal scatter within the spectrometer portion of that instrument (Jeffery Warren, personal communication; Howser 2002). Light from wavelengths up to hundreds of nanometers out-of-band was found to contaminate any given CRISP spectrometer channel, including "dark" pixels positioned outside the nominal light path. The effect was attributed to scatter from the spectrometer grating. The individual contamination of light at any one wavelength to the detectors of another was small (i.e., less than 1% of the in-band signal), but the aggregate effect of all out-of-band wavelengths inflated the apparent signal in all channels. The effect was greatest in the channels that measured the lowest radiances (i.e., the longest wavelength channels) and required correction for proper calibration of the instrument. NIS calibration did not incorporate a scattered light correction from pre-flight tests. The removal of a grating

scatter effect, if present in NIS, may improve NIS calibration and data quality.

Initial analysis of NIS ground calibrations showed that internal scattering effects were likely to be of the same order as off-axis response; 0.1% or less (Fig. 29 in Warren et al. [1997]). To determine internal scatter in NIS and, if present, whether it is responsible in whole or in part for the red slope observed at Eros, we revisited the ground calibration data and discovered nontrivial scattered light within the instrument not accounted for in instrument calibrations.

NIS ground calibration tests included a wavelength calibration in which a monochromator delivered light to the instrument in narrow (~4–5 nm band) increments (NIEML05 in Table 2). The monochromator center wavelength was scanned in 10 nm increments from 750 to 1500 nm and 20 nm increments from 1500 to 2700 nm. This wavelength scan was used to determine the NIS channel bandpasses in Warren et al. (1997).

In both Ge and InGaAs detectors, most individual channels receive small amounts of light from both near- (tens of nm) and far-wavelengths (hundreds of nm). Incoming light at a given wavelength is scattered off the grating, causing some of it to fall onto detectors out of the intended band. Examples are shown in Fig. 2. The near-wavelength effect is most significant in immediately adjacent channels and is stronger in the InGaAs detector. The far-wavelength contamination, most noticeable in the Ge detector, is small on a per wavelength basis, but can sum to an appreciable effect. Far-wavelength effects are also amplified when wavelengths with higher radiance scatter into channels that normally receive lower radiance (e.g., longer wavelength channels in InGaAs).
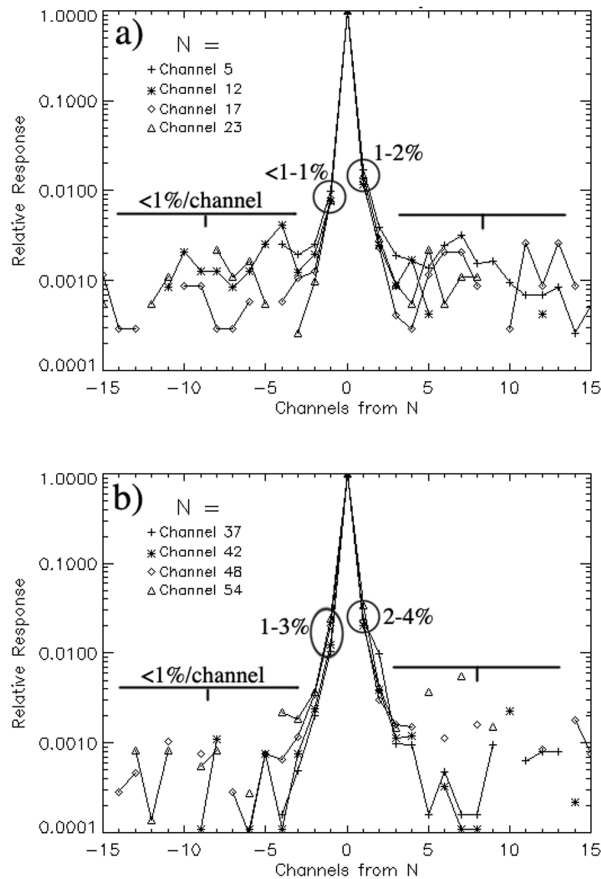

Fig. 2. Plots of channel-to-channel relative response in the NIS detectors showing near and far wavelength scattered light. Channels are offset to overlap and scaled to 1 at the maximum signal, where a ground calibration monochromator wavelength is centered on channel bandpass: a) four representative channels in the Germanium detector (~800–1500 nm); b) four representative channels in the Indium-Gallium-Arsenide detector (1400–2500 nm). Near-wavelength scattered light (circled) is on the order of <1–5%, greater from the N + 1 channel wavelength than the N − 1 channel and more pronounced in the InGaAs detector than in Ge. Far-wavelength scattered light is under 1% per channel in both detectors, but the combined effect is up to 1% or more on a given channel, most pronounced in the higher signal Ge channels.

The near-wavelength scatter was determined using band passes in the monochromator scan that were well centered on a given NIS channel (i.e., the monochromator 900 nm band pass fell in the middle of the 22 nm-wide NIS channel 5, centered at 902.7 nm). The signal at a given NIS channel N was contaminated by the addition of 1–5% of the signal from channel N − 1 and 0.7 to 4% of the signal of channel N + 1. The effect was about twice as strong in the InGaAs detector as in the Ge, and both detectors tended to have a greater scatter from light in the wavelength range of the N − 1 channel than from N + 1. This asymmetry is attributed to the asymmetric blazing of the toroidal Rowland circle spectrometer grating (Warren et al. 1997). Near-wavelength contamination is roughly an order of magnitude greater than the off-axis response at 0.5° (Fig. 29 of Warren et al. [1997]). Scattered light is reduced by a factor of several to an order of magnitude at wavelengths 2 channels away (N ± 2) and, in general, to 0.1% or less at distant wavelengths (|N| >2). The far-wavelength scatter is, on average, a DN or less per channel above the noise for signals of several hundred to a few thousand DN (Fig. 2), but summing over all wavelengths in the detector yields an out-of-band signal up to several percent.

The removal of instrument scattered light is accomplished by generating a "scrubbing" filter from ground calibration data. The near-wavelength component of the filter is generated by taking the set of well matched monochromator and NIS wavelengths (e.g., 1140 nm for channel 16 at 1140.4 nm), determining the near-neighbor scattered light out to N ± 3 for each, and interpolating for NIS channels that do not have well matched monochromator data (e.g., channel 20 at 1226.8 nm). The far-wavelength component is determined by interpolating the dark-subtracted data for channels beyond N ± 3 across the monochromator scan range to the 64 NIS channel wavelengths. The results of the interpolation are a 32 × 32 channel versus a wavelength matrix of relative response for each NIS detector (see Appendix A). Summing all out-of-band contributions for a given NIS channel N and subtracting that sum of scattered light from the signal at channel N, we derive the final filter for a given spectrum:

$$R'_{(\lambda = N)} = R_{\lambda = N} - \sum F_{(\lambda = N, \lambda \neq N)} \bullet R_{\lambda \neq N} \qquad (1)$$

where $R'_{(\lambda = N)}$ is the net response at a given NIS channel N, $R_{\lambda = N}$ is the measured response at that channel, $F_{(\lambda = N, \lambda \neq N)}$ is the out-of-band response array for channel N, and $R_{\lambda \neq N}$ is the response of channel N to light from other wavelengths.

Ideally, Equation 1 is to be applied to the NIS radiance calibration coefficients and incorporated into a revised calibration equation. However, for the purposes of correcting the already calibrated, photometrically corrected, and publicly released data set used in this study, we derive an intermediate approach. Filtering the end product NIS spectrum alone is insufficient because the scattered light affects the calibration coefficients used to convert instrument

counts to radiance values. The scattered light on all detectors means that fewer counts in a given channel represent a given radiance value, and, therefore, the radiometric conversion (DN per unit radiance) has been over-estimated. To compensate for this after-the-fact, we apply the filtering matrices twice: first to the dark-subtracted, crosstalk corrected, normalized spectrum from on-ground calibration used to determine the radiometric coefficients for NIS (Warren et al. 1997; Izenberg et al. 2000a), and second to an average Eros spectrum observed on orbit. This before-and-after correction is reduced to a single vector of corrections applied to calibrated NIS data using the relationship:

$$\text{scalar correction}_\lambda = \frac{\text{ground spectrum}_\lambda}{\text{ground spectrum filtered}_\lambda} \bullet \frac{\text{avg. Eros filtered}_\lambda}{\text{avg. Eros}_\lambda} \quad (2)$$

where the "ground spectrum" is taken from the radiometric calibration observations of a gold-coated integrating sphere during on-ground calibrations (NIGRL10 in Table 2), and the "average Eros" spectrum is taken from the high-resolution observations of Eros (observation phases M and N in Table 2) and photometrically corrected to a uniform incidence angle (i) of 30° and emission angle (e) of 0°. The correction we use is a 5th order polynomial fit to the result of Equation 2, applied by multiplication to calibrated, photometrically corrected NIS spectra. The relative response matrices and derived scattered light correction coefficients are shown in Appendix A. The effects of scattered light removal on NIS spectra and derived parameters are shown in Fig. 3.
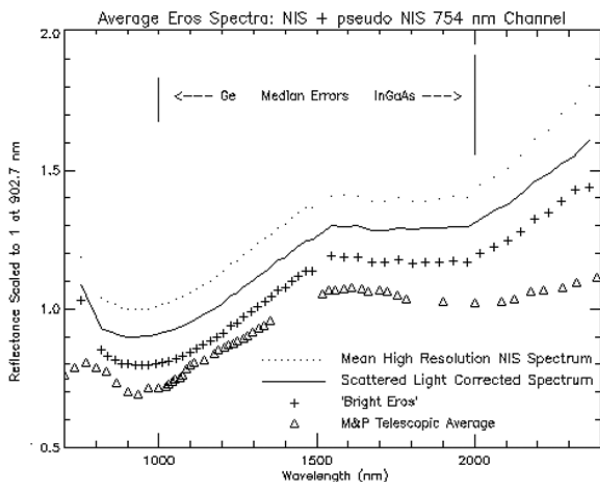

Fig. 3. Average Eros spectra from the 3127-spectrum NIS+ data set, with (solid line) and without (dotted line) scattered light correction. Also shown is the average "bright" Eros spectrum (see Table 5), and the average telescopic spectrum of Eros from Murchie and Pieters (1996). Spectra are normalized to 1.0 at 900 nm and linearly displaced by offset steps of 0.1 at 900 nm. The error bars are per measurement for representative channels in the Ge and InGaAs detector. Deviation around the mean of the average spectrum is on the order of the line thickness of the plot. Scatter-corrected NIS spectra show, on average, slightly reduced red slope, longer wavelength band centers, decreased band depth, and smaller BAR.

Extending Effective NIS Spectral Range With MSI

Once spectra and images are calibrated, photometrically corrected to a uniform viewing geometry, and "scrubbed" of scattered light, the addition of shorter wavelength information, in this case from MSI filter 3 at 754 nm, to NIS spectra can create a more complete near infrared spectrum to better characterize Eros' surface composition using band parameters. The shortest wavelength channel on the NIS instrument is centered at 816 nm, which is inside the Fe^{2+} electronic transition absorption feature that defines Band I in many iron-bearing silicate minerals, such as olivine and pyroxene (Adams 1974; Cloutis et al. 1986). Band parameter determination, and thus mineralogical interpretation, using this curtailed wavelength range is dependent on model-based or empirical corrections. Earlier work using NIS-only spectra relied on such corrections to enable comparison of NIS data with astronomical observations of Eros, other asteroids, and laboratory measurements of meteorites. McFadden et al. (2001) and Bell et al. (2002) relied on corrections to NIS-only spectra derived from early NIS + MSI spectrum extension work (Izenberg et al. 2000b, 2001) and from comparing NIS data to model and laboratory spectra intentionally cut off at shorter wavelengths to mimic the NIS spectral range (Michael Gaffey, personal communication).

In many minerals, including those prevalent in meteorites used as asteroid analogues in laboratory measurements (e.g., Gaffey et al. 1993), the short wavelength "shoulder" of Band I extends to wavelengths 700 nm or shorter. In telescopic studies of asteroids, particularly the S-type groups of which Eros is a member, the Band I shoulder, crucial for determining band continuum slope, ranges from near 700 nm to near 800 nm (Gaffey et al. 1993). This end of the shoulder is critical in deriving Band I spectral parameters. Adding 754 nm data by including values from MSI filter 3 effectively completes Eros' short wavelength Band I shoulder and should, thus, decrease uncertainty when comparing Eros data to full-spectrum telescopic asteroid spectra and laboratory meteorite spectra.

Izenberg et al. (2000b, 2001) first explored the application of MSI spectral data to extend the NIS spectrum below 816 nm. Initial efforts focused on the location of simultaneously acquired NIS and MSI data and simple appending of the MSI filter 3 (754 nm) radiance factor (I/F = intensity of reflected light/specific solar radiance) data to NIS spectra, where MSI filter 4 (951 nm) I/F was within ±2% of that in NIS channel 7 (945.9 nm) and where both data sets were photometrically corrected to the same viewing geometry. The matching yielded approximately 490 spectra from the NIS high-resolution data set. The analysis produced spectral band parameters closer to telescopic results for Eros and laboratory results for analogue meteorites without the need for added correction factors, implying that adding the

Table 2. NIS data used in this investigation.

Phase	Description	Dates	MET range[a]	Subphases	Notes
NIEML05	Wavelength calibration	07–13–1995	–	Ground calibration	Monochromator scans over NIS wavelength range.
NIGRL10	Radiometry	07–14–1995	–	Ground calibration	Radiometric calibration using gold-coated integrating sphere.
NILRL11, 12	Radiometry	07–13–1995	–	Ground calibration	Radiometric calibration using white (BaSO$_4$) integrating sphere.
M	100–50 km transfer orbit	04–24–2000 to 05–03–2000	131887500 to 132635799	MA-MU	Multiple observation types. Lowest-altitude data used in high-resolution data set.
N	Low orbit I (50 km)	05–04–2000 to 05–14–2000	132635800 to 133618899	NA-NB	NIS ceased function on May 14, 2000.

[a]MET is mission elapsed time in seconds. Zero time is NEAR launch: February 17, 1996 20:43:30.628 UT.

short wavelength data to the NIS spectrum improves the range and reliability of NIS observations and suggesting that brightness-based and geology/morpholgy-based spectral differences on Eros could be further explored with an extended spectrum. However, NIS and MSI, each with different exposure times, gains, and instrument noise, can differ significantly in absolute reflectance across Eros, especially if the data were not simultaneous or were taken with very different viewing geometries. The data set matched in this most basic and restrictive fashion is small and geographically constrained, mainly to the average Eros cratered plains regions.

To expand the size and geographic coverage of the fused data set, a synthetic or "pseudo" channel at 754 nm is derived for NIS using the MSI "950/760 ratio" from Murchie et al. (2002a), applied to NIS channel 7 (945.9 nm) data:

$$NIS_{754} = \frac{MSI_{754}}{MSI_{951}} \bullet NIS_{945.9} \qquad (3)$$

where NIS_{754} is the derived reflectance for NIS at 754 nm; MSI_{754} and MSI_{951} are reflectance for MSI filters 3 and 4, respectively (the 760 and 950 used in Murchie et al. [2002a] are the nominal filter center wavelengths, 754 and 951 are the effective centers from on-ground calibrations described in Appendix C of Murchie et al. [1999]), and $NIS_{945.9}$ is the NIS channel 7 reflectance. Using color ratio data removes the absolute differences between NIS and MSI and provides a more reliable and consistent solution that can be applied successfully to more NIS spectra.

We explore the sufficiency of extending the NIS spectrum to 754 nm by comparison with telescopic observations of Eros and laboratory observations of chondritic meteorites. In Appendix B, we show the effect of cutting off, at various wavelengths, the short-IR end of telescopic and meteorite spectra. Compared to a cutoff at 816 nm, extension to 754 nm results in a ~3–12 nm shortening of the Band I center wavelength and a significant decrease in BAR (0.2–0.5) due to the effective increase in Band I area. Were we able to extend NIS-type observations to even shorter wavelengths, the effect on band parameters for Eros would be

negligible to slight. Assuming typical ordinary chondritic mineralogy, the Band I center wavelength, for example, could vary up to +10 nm from the fused spectrum. The band area ratio could decrease by up to −0.02. Assuming a spectrum more like Band 1 in the Murchie and Pieters (1996) telescopic average for Eros does not extend much shorter than 750 nm and that the spectrum is generally representative of Eros, extending coverage to even shorter wavelengths would have no additional effect on band parameters.

Data Sampling

We created a database from the highest resolution calibrated NIS spectra acquired from orbit phases M and N during the Spring of 2000 (Table 2). The footprint size ranges from 213 × 427 m to 394 × 788 m. Only fully illuminated NIS footprints were included (i.e., spectra that sampled the terminator and limb as determined by the Eros shape model in Thomas et al. [2002] were eliminated). To reduce possible photometric effects, only spectra with incidence angles of 75° degrees or less were used. The terminator, limb, and high incidence angle exclusions all decrease the occurrence of heterogeneity within the NIS footprint, reducing the sub-footprint spectral variation problems described in Izenberg et al. (2000a) and McFadden et al. (2001). The remaining sources of heterogeneity within the NIS footprint include small-scale topography and brightness variations. To reduce the impact of instrument-specific resolution and photometry differences, NIS and MSI data with absolute reflectance differing by a factor of ~2 were not considered. All spectra were photometrically corrected to an incidence angle of 30°, and an emission angle of 0° (Clark et al. 2002). The NIS database was culled to exclude the noisiest data, eliminating spectra with detector noise greater than 30% of the signal (SNR worse than ~3.4). The after-the-fact scattered light correction described above was applied to the remaining spectra.

The MSI data used to generate the NIS 754 nm pseudo channel were 3° × 3° maps of MSI reflectance at 754 nm (filter 3, Fig. 1b) and 951 nm (filter 4, Fig. 1a) and color ratio generated from Eros approach imaging in February 2000

(Murchie et al. 2002a). These maps are photometrically corrected to i = 30° and e = 0°. The MSI approach maps primarily cover the northern hemisphere of Eros, while NIS high-resolution coverage extends substantially southward (to below 60° S under Psyche and 45° S under Himeros). Excluding locations where filter 3 reflectance standard deviations were 0.025 or greater eliminated the least reliable MSI data (Fig. 10, Murchie et al. 2002a)

To co-locate NIS and MSI spectral data, we systematically paired each NIS spectrum with corresponding values from the MSI maps. NIS footprints are matched by center latitude and longitude to MSI data at the same coordinates. The data are further cut to eliminate "degenerate" band parameter solutions (i.e., where automated polynomial fitting of Band I and Band II produced overlapping bands). The resulting data set contains 3127 extended spectra, which we refer to as the "NIS+ data set" or simply "NIS+." Coverage of the data set ranges across the northern hemisphere of Eros, dipping below the equator at Psyche and Himeros (Fig. 4). Most NIS+ locations are covered by 1 or 2 spectra, with some areas, most notably north of the 180° longitude nose and to the east of Psyche, having multiple spectra due to repeated coverage on-orbit. Even though Psyche and Himeros rims are well observed by NIS, few observations exist where NIS and MSI both have high SNR data for inclusion in the NIS+ set.

Spectral Parameters

We calculate spectral parameters for the NIS+ data set: continuum slope, absorption band center, depth, area, and BAR from individual spectra, global average, and selected

subgroupings of the global set. Bell et al. (2002) provides an overview of the significance of spectral band parameters and their uses in interpretations. We derived band parameters using methods similar to McFadden et al. (2001) and Bell et al. (2002), which are summarized in Table 3. For continuum slope determinations, we used the tangent method described in McFadden et al. (2001). We found band centers derived from 4th to 6th order polynomial fits of the continuum-removed absorption band features to be generally better (i.e., having lower chi-squared values) than the typical 3rd to 5th order solutions (Gaffey et al. 1993; Bell et al. 2002).

RESULTS

All band parameters derived and discussed below are of the NIS+ data set with the pseudo-NIS channel at 754 nm added. All spectra presented from this study have the scattered light correction applied unless otherwise indicated. No empirical or other adjustments are made to any of the spectral parameters derived from NIS+; they are directly compared with other meteorite and asteroid data.

Average Spectral Properties

An average high-resolution spectrum from the NIS+ data set is shown in Fig. 3, both with and without the scattered light correction, compared to the Murchie and Pieters (1996) telescopic average. We derive the average spectrum by co-adding all measurements for a given channel and dividing by the number of observations (3127 for the full NIS+ data set). The error bars shown are standard deviations of 3127 measurements in each channel for representative channels in
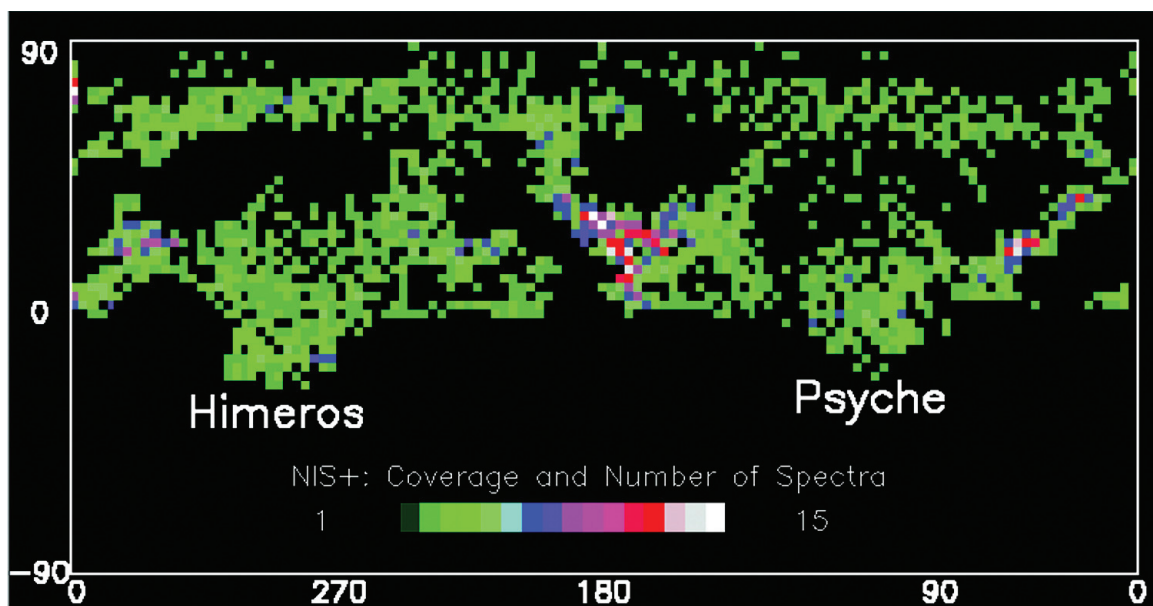

Fig. 4. Map showing coverage and density of observations for the NIS+ data set on Eros. Each box is a 3° × 3° bin on a simple cylindrical projection of Eros, after Murchie et al. (2002a).

the Ge and InGaAs detectors and do not represent channel-to-channel variation, which is very small. The average spectrum has a much higher SNR than any individual spectrum (SNR levels vary by channel, detector, and light level but generally range from 3–15 for this data set), and parameters derived from the average spectrum are, therefore, more representative of average Eros than the mean of parameters of all the individual spectra in the data set, which are also shown in Table 4.

Though Band I parameters and BAR for NIS+ are not directly comparable to earlier NIS work due to the addition of the derived 754 nm pseudo-channel, the average NIS+ Eros spectrum without scattered light correction (plotted as the dotted line in Fig. 3 and shown in parentheses in Table 4) is consistent with previously published NEAR data (McFadden et al. 2001; Bell et al. 2002). The extended NIS spectrum makes for a shallower near-IR slope, greater Band I depth, and smaller BAR (Table 4). The scatter-corrected average NIS+ spectrum (solid line in Fig. 3) differs from the uncorrected extended spectrum with shallower spectral slopes, longer wavelength band centers, shallower band depths, and a significantly smaller BAR. The greatest effects of scattered light removal are reduced BAR and longer wavelength Band I center due to broadening the long-wavelength side of the Band I absorption feature. The reduction in red slope to the NIS+ average spectrum from scattered light correction is minor with respect to the absolute difference in red slope between the NIS+ and telescopic average spectrum of Eros (Murchie and Pieters 1996).

The derived NIS pseudo channel at 754 nm stands out in Fig. 3's average spectrum plot due to a 62 nm gap between it and NIS channel 1 at 816 nm. The coarseness of this sampling

Table 3. NIS Spectral Parameters.

Parameter	Description	Note[a]
Band I slope	Change in I/F in 1000 nm neighborhood divided by the change in wavelength for spectra normalized to 1.0 at NIS channel 1 (816 nm).	I
Band I center	Least chi-squared solution of a 4th to 6th order polynomial fit of linear continuum-removed spectrum in the 1000 nm region.	II
Band I depth	1.0 minus the value of continuum removed spectrum at the wavelength of the Band I center.	II, III
Band II slope	Change in I/F divided by the change in wavelength for spectra normalized to 1.0 at NIS channel 1 (816 nm).	I
Band II center	Least chi-squared solution of a 4th to 6th order polynomial fit of linear continuum-removed spectrum in the 2000 nm region.	II
Band II depth	1.0 minus the value of continuum removed spectrum at the wavelength of the Band II center.	II, III
Band area ratio (BAR)	Ratio of integrated area of Band II to integrated area of Band I (areas are from the polynomial fits between respective band's continuum points).	III
Reflectance	Calibrated I/F at a given wavelength photometrically corrected to $i = 30°$, $e = 0°$ using the model in Clark et al. (2002).	

[a]I. Ni-Fe metal abundance. Degree of space weathering (Cloutis et al. 1990; Clark 1995; Gaffey and Gilbert 1998; Hapke et al. 1975; Allen et al. 1993; Pieters et al. 2000). II. Fe^{2+} electronic absorption features. Olivine/Pyroxene chemistry/mineralogy variations (Gradie and Veverka 1986; Cloutis et al. 1986; Cloutis and Gaffey 1991). III. Pyroxene composition, grain size, olivine/pyroxene ratio, viewing geometry effects (Adams 1974; King and Ridley 1987; Cloutis and Gaffey 1991).

Table 4. Table of derived NIS parameters ±1σ.

Parameter[a]	This study		Previous averages		
	3127 NIS+ spectra	Average Eros[b]	Murchie and Pieters (1996)	McFadden et al. (2001)	Bell et al. (2002) LPF[c]
B-I slope	0.279 ± 0.046	0.267 ± 0.008 (0.293)	0.368 ± 0.015	0.473 ± 0.135	0.58 ± 0.15
B-I center (nm)	969 ± 22	962 ± 6 (946)	969 ± 15	952 ± 24	971 ± 13
B-I depth (%)	19.2 ± 1.2	18.9 ± 0.1 (19.2)	19.0 ± 1.0	11.2 ± 1.9	17.2 ± 0.8
B-II slope	0.383 ± 0.077	0.372 ± 0.005 (0.477)	–	–	0.55 ± 0.16[d]
B-II center (nm)	1974 ± 33	1968 ± 10 (1963)	2000 ± 100	1990 ± 14	1994 ± 19
B-II depth (%)	11.4 ± 2.2	9.5 ± 0.2 (12.1)	–	–	11.3 ± 0.5
BAR	0.60 ± 0.16	0.51 ± 0.02 (0.67)	0.62 ± 0.12	0.77 ± .18	0.79 ± 0.19
902.7-nm I/F	0.101 ± 012	0.101 ± .012 (0.998)	–	–	0.234 ± 0.034[e]
opx/(opx + olv)[f]	0.34 ± 0.08	0.31 ± 0.02	0.3 ± 0.1	0.42 ± 0.04	0.42 ± 0.08[g]

[a]Parameters calculated using NIS+ pseudo-NIS data with scattered light correction applied.
[b]Values in parentheses are for average NIS+ spectrum without scattered light correction.
[c]Band parameters for spectra photometrically corrected to $i = 0°$, $e = 0°$.
[d]As defined in Fig. 10 in Bell et al. (2002).
[e]Normal albedo from Clark et al. (2002).
[f]Using Cloutis et al. (1996) olivine to pyroxene mixing calibration, modified by McFadden et al. (2001).
[g]Based on reported average band area ratio of 0.79 ± 0.19.

at the short wavelength end of Band I may have an effect on its curve fitting, but the polynomial fits of this part of the spectrum, described in Table 3, tend to be smooth and consistent.

Synoptic Observations

NIS, like MSI, reveals variations in reflectance across Eros' surface, though at a lower fidelity than the imager due to coarser spatial resolution; photometric corrections over larger and less-uniform ranges of (i), (e), and phase angle between different observations; and non-uniformity of photometry within individual NIS spectra. Variations in NIS brightness data (represented in Fig. 5 by NIS 902.7 nm I/F) are generally similar to those shown by MSI 951 and 754 nm (Figs. 1a and 1b). Fig. 6a shows the MSI 754 nm data restricted to the coverage of the NIS+ data set. The south rim of Psyche and the region north of Himeros differ notably in reflectance values between NIS and MSI. NIS reflectance in these areas relative to the rest of the asteroid is substantially higher than seen by MSI. In both cases, the Eros shape model (Thomas et al. 2002) used to derive the photometric corrections (Clark et al. 2002) probably does not fully account for the topographic complexities of these locations (e.g., the topography of south Psyche rim, which includes several smaller craters in its vicinity, and the Rahe Dorsum ridge, which arcs above Himeros). The MSI 754 nm reflectance in the NIS+ coverage has the full 0.08 to 0.27 range seen in Murchie et al. (2002a), with a mean of 0.13. As in the full data set, 95% of the MSI data in NIS+ fall between 0.09 and 0.22

(a factor of 2.5 variation). NIS 902.7 nm reflectance ranges from 0.04 to 0.23, and 95% of the NIS reflectance data fall between 0.08 and 0.13 (a factor of 1.6 variation).

Band I depth, determined by the relationship between the continuum-removed spectrum and the reflectance of the Band I center (Table 3) is inversely related to color ratio. Because the MSI color ratio (Fig. 6b) was used to determine the NIS 754 nm pseudo-channel, color variations represented by NIS+ Band I depth (Fig. 6c) bear a strong inverse resemblance. Ninety five percent of the MSI color ratio varies in NIS+ coverage between 0.81 and 0.88. Band I depth in NIS+ varies between 0.17 and 0.22. The lowest MSI ratios (below 0.84) and deepest Band I depths (above 0.21) lie at the equator and "noses," along the rim and North wall of Psyche, and along the southeast rim of Himeros. High MSI ratios and shallow Band I depths occur in the interiors or floors of Psyche and Himeros and to a lesser extent at the north end of the 180° longitude nose and the region north of the Psyche rim.

Band I center (Fig. 6d) and slope show correlations with Eros surface features similar to Band I depth. The slope image is not shown because it is very similar to Fig. 6d. Psyche interior, Himeros interior, the equator, and the 180° nose all stand out with longer wavelength band centers (yellow-red-white colors in Fig. 6d) and steeper near-infrared slopes. Shorter wavelength Band I centers (blue colors) and shallower slopes are present around parts of the equator, the rims of Psyche and Himeros, and areas north of psyche near the pole. Maps of Band II parameters and BAR show little obvious correlation with morphologic features. The noisiness of the NIS spectrum at the longer wavelengths makes it
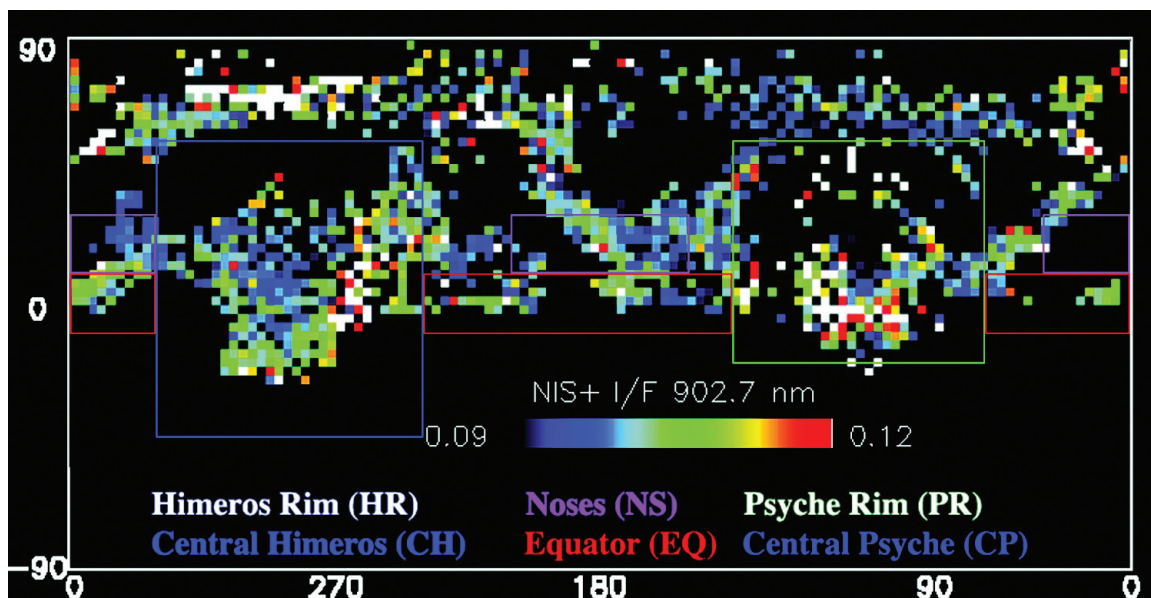

Fig. 5. NIS reflectance (I/F) at i = 30°, e = 0°, 902.7 nm (channel 5) for the NIS+ data set. Geographic/Morphologic regions used to subdivide the NIS+ data set are shown in the background. Central Psyche (CP) and Psyche rim (PR) are discriminated by high and low reflectance materials within the Psyche region (green box). Central Himeros (CH) and Himeros rim (HR) are similarly determined (blue box). Noses (NS) and Equator (EQ) are determined by latitude and longitude boundaries.
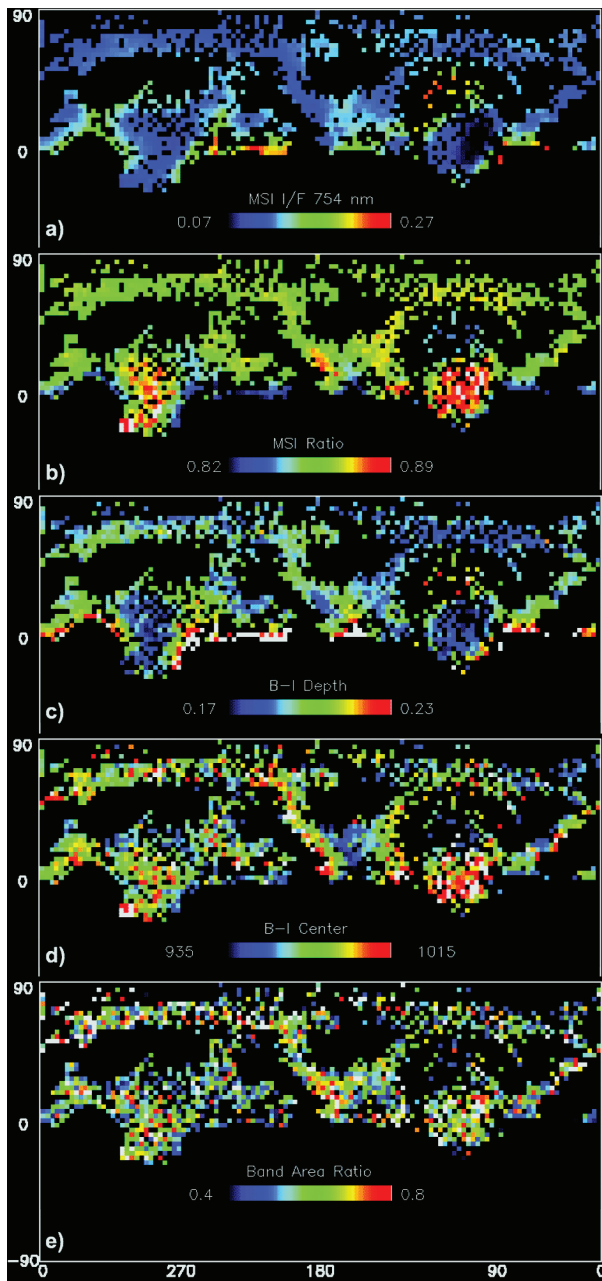
Fig 6. A series of NIS+ parameter maps: a) MSI reflectance (I/F) at i = 30°, e = 0°, 754 nm (filter 3) from Fig. 1 restricted to NIS+ data set coverage. Reflectance differs significantly between MSI and NIS in Psyche and north of Himeros; b) map of MSI 951 nm/754 nm color ratio (from Murchie et al. 2002). Color ratio is inversely related to Band I depth. The MSI color ratio is higher in the interiors of Psyche and Himeros and near the 180° nose. Low color ratios are present along the equator and the Psyche and Himeros rims; c) NIS+ Band I depth. The anti-correlation with MSI color ratio is strong, in part because the 754 nm pseudo channel used to extend the NIS spectrum is derived from it; d) the NIS+ Band I center map shows longer wavelengths in the interior of Psyche and Himeros and shorter wavelengths near the rims and Eros equator. The Band I slope map (not shown) is similar; e) the NIS+ band area ratio map does not show the weak correlations seen in Bell et al. (2002). Higher BAR may be seen in interior Psyche and near the noses of Eros.

difficult to discern global patterns in Band II parameters. The weak correlations for Band II depth and BAR, seen in low phase flyby data from Bell et al. (2002), most notably in the equatorial region and the south rim of Psyche, are not present in the synoptic views of NIS+ data. Higher band area ratios may be present in the interior of Psyche and near the 0° and 180° noses (Fig. 6e).

Global Spectral Variations

We examine the full NIS+ data set for correlations among spectral parameters following methods similar to Bell et al. (2002). We generate a series of two-dimensional correlation plots (or 2D-histograms) comparing parameters against each other for the entire NIS+ data set and 2 subsets discriminated by I/F (Table 5). Separately, we compare subsets of geographically and morphologically distinct areas on the asteroid (Table 6).

The brightness-dependent subsets of NIS+ are selected on the basis of reflectance of both NIS and MSI as shown in Table 5. The "bright" data set contains 27 spectra where NIS channel 5 I/F (902.7 nm) is above 0.11 and MSI filter 3 (754 nm I/F is above 0.19. The spectra in this subset are located mainly on the wall of Psyche, with a handful at the equator east of Himeros, and also in bright crater wall materials. The "dark" subset has the converse selection criteria, and contains 2450 spectra spread across much of the asteroid. Spectra with highly divergent NIS and MSI reflectances (~21% of the NIS+ set) were not included in brightness subsets. The eliminated spectra are inferred to represent either NIS spectra with sub-pixel shadowing or cases in which the photometric corrections are inaccurate. The parameters of the average dark subset spectrum (Table 7) differ little from those of the average Eros spectrum (Table 4).

Figure 7 shows comparisons of band parameters for the NIS+ data set and the bright and dark subsets. In each plot, the derived parameters of all 3127 NIS+ spectra are shown as a cloud of points. Scatter is primarily a function of signal-to-noise ratio. The mean parameters of the dark and bright subsets (e.g., the means of 2450 dark and 27 bright Band I center values) are shown as small triangles and squares, respectively, with 1σ error bars. The parameters of the average spectrum for the dark and bright subsets (e.g., single spectra created by averaging 2450 dark spectra, and all 27 bright spectra, as shown in Table 7) are shown as large triangles and squares. In general, the parameters of the average spectrum are preferred over the mean parameters due to their significantly higher SNR.

Figure 7a shows a plot of Band I center versus Band II center. The plot range covers the lower half (of the Band II range) of the ortho- and clino-pyroxene ranges observed in laboratory samples (Adams 1974; Cloutis et al. 1986). The NIS+ Eros data cluster in generally the same area as the LPF data in Bell et al. (2002): near the orthopyroxene to low-

Table 5. Reflectance-discriminated subsets of the NIS+ data set.

Discriminator (N)	NIS channel 5 (902.7) I/F[a]	MSI filter 3 (754 nm) I/F[b]	Spectra in subset
Bright Eros[c]	N >0.11	N >0.19	27
Dark Eros	N <0.11	N <0.19	2450

[a]See Fig. 5.
[b]See Fig. 6a.
[c]This subset contains bright crater wall material, mostly from Psyche, and craters near the equator.

Table 6. Geographic/Morphologic subsets of the NIS+ data set.

Subset name	Location[a]	Latitude	Longitude	Discriminators	# of spectra
Central Psyche (CP)	} Psyche	−20° < N < 5°	50° < N < 135°	Dark[b]	52
Psyche rim (PR)				Bright[c]	17
Central Himeros (CH)	} Himeros	−40° < N < 60°	250° < N < 330°	Dark[b]	39
Himeros rim (HR)				Bright[c]	19
Equator (EQ)	Equator	−10° < N < 10°	N = 0° − 360°	Excludes Psyche and Himeros	224
Noses (NS)	Noses	N <30°[d]	330° < N < 30° and 150° < N < 210°	Excludes equator	491

[a]See also Fig. 6.
[b]Low reflectance floor materials (Murchie et al. 2002a). NIS channel 5 I/F <0.10, MIS filter 3 I/F <0.11.
[c]High reflectance wall and rim materials. NIS channel 5 I/F >0.10, MIS filter 3 I/F >0.18.
[d]No NIS+ spectra lie south of the equator.

Table 7. Derived spectral parameters of the NIS+ subsets.

Parameter	Bright Eros	Dark Eros	Equator	Noses
BI slope	0.184 ± 0.011	0.272 ± .002	0.241 ± 0.001	0.279 ± 0.005
BI center (nm)	958 ± 5	961 ± 3	963 ± 6	957 ± 8
BI depth (%)	21.7 ± 0.3	21.7 ± 0.3	20.4 ± 0.1	1 8.9 ± 0.2
BII slope	0.301 ± 0.032	0.380 ± 0.021	0.350 ± 0.002	0.393 ± 0.001
BII center (nm)	1965 ± 4	1968 ± 2	1962 ± 4	1969 ± 3
BII depth (%)	9.7 ± 0.5	9.5 ± 0.2	9.6 ± 0.6	9.7 ± 0.2
BAR	0.43 ± 0.06	0.51 ± 0.02	0.48 ± 0.2	0.52 ± 0.03
902.7 nm I/F	0.120 ± 0.010	0.098 ± 0.007	0.102 ± 0.010	0.099 ± 0.011

Parameter	Central Psyche	Psyche rim	Central Himeros	Himeros rim
BI slope	0.319 ± 0.018	0.206 ± 0.012	0.305 ± 0.008	0.173 ± 0.024
BI center (nm)	981 ± 4	961 ± 3	987 ± <1	951 ± 1
BI depth (%)	17.5 ± 0.5	20.7 ± 0.3	17.4 ± <0.1	22.9 ± 1.1
BII slope	0.383 ± 0.40	0.346 ± 0.014	0.366 ± 0.043	0.307 ± 0.024
BII center (nm)	1969 ± 4	1970 ± 7	1968 ± 2	1960 ± 6
BII depth (%)	9.8 ± 0.5	10.2 ± 0.6	10.0 ± 0.5	9.4 ± 1.0
BAR	0.58 ± 0.03	0.51 ± 0.03	0.57 ± 0.04	0.40 ± 0.04
902.7 nm I/F	0.094 ± 0.004	0.115 ± 0.011	0.095 ± 0.004	0.110 ± 0.008

calcium clinopyroxene end of Adams' (1974) band correlation diagram and in the S(IV) to S(V) classifications of the Gaffey et al. (1993) taxonomy. Bright subset data have slightly shorter Band I centers than the dark subset, and the average spectra plot lower in both parameters than the mean of the cloud of points. The average bright Band II center is several nm shorter than the average dark. This variation is small with respect to the pyroxene variations in Adams (1974) and Cloutis et al. (1986).

Figure 7b shows Band I depth versus Band II depth. Variation in band depth is generally small (Tables 5 and 8), but Band II depth scatter is greater than that of Band I depth due to the generally lower signal-to-noise of the longer wavelength InGaAs detectors (Izenberg et al. 2000a). Bright subset spectra plot out of the main cloud of data with several percent greater Band I depths. When the individual spectra are combined to produce the average spectrum, the improved signal-to-noise ratio reduces scatter and decreases the overall Band II depth. The greater band depth of bright Eros—primarily crater wall material—is consistent with MSI observations and the MSI 950/760 ratio variations in Murchie et al. (2002a) and Robinson et al. (2002). No such correlation was apparent in the low phase flyby data (Bell et al. 2002), which was likely due to poor spatial resolution and the
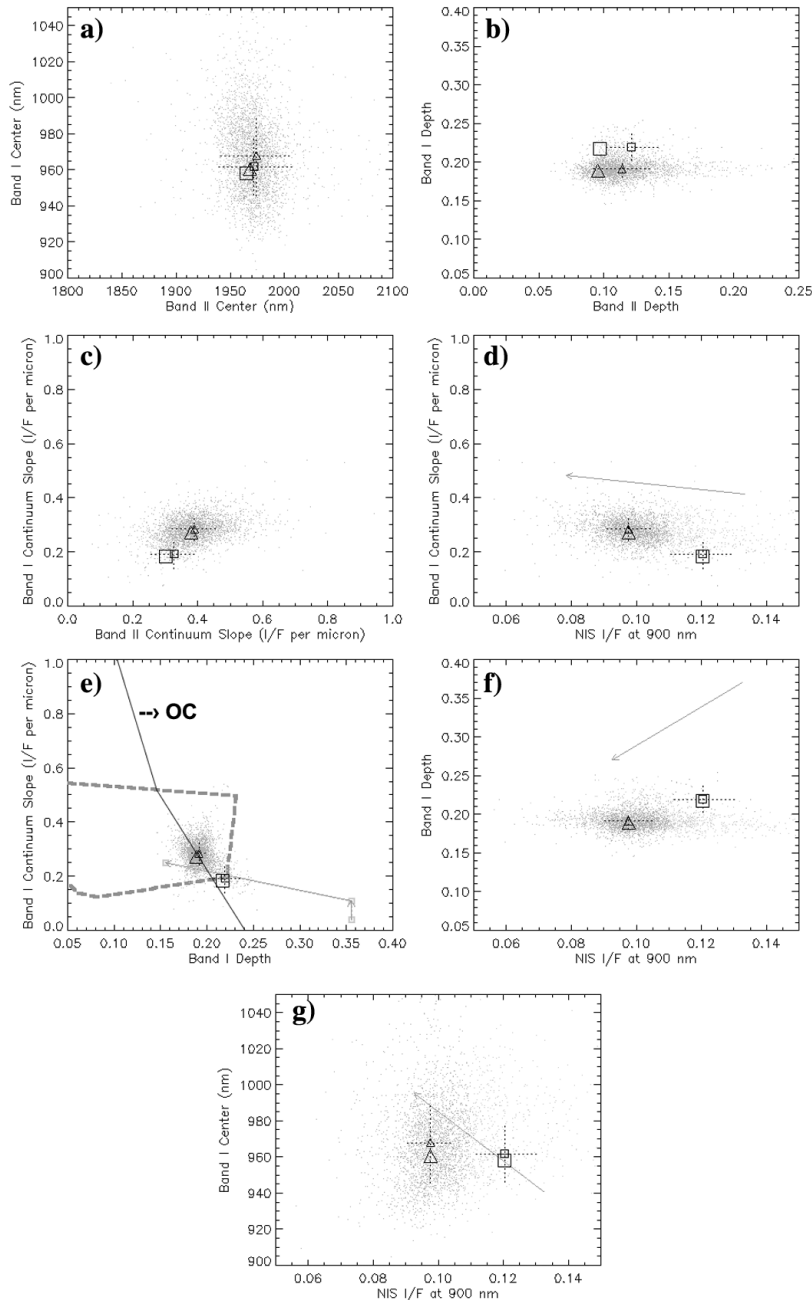
Fig. 7. Band parameter correlation plots for the NIS+ data set and bright and dark subsets. The cloud of points shows individual parameters for the full 3127-spectrum NIS+ data set. The small squares represent the mean of the parameters of the 27 individual spectra comprising the bright subset, with 1σ error bars. The large square shows the derived parameters of the single average bright spectrum from Table 7 (with error bars smaller than the symbol size). The large and small triangles show the dark NIS+ subset parameters using the same scheme: a) Band II center versus Band I center shows that the bright subset data have slightly shorter band centers than the dark. High SNR average spectra result in shorter wavelength Band II center; b) Band II depth versus Band I depth shows bright materials have deeper Band I depths. The increased SNR of the average spectra results in shorter Band II; c) Band I continuum slope versus Band II continuum slope shows bright materials have shallower slopes. Darker materials have steeper slopes and appear spectrally more red; d) NIS reflectance at 902.7 nm versus Band I continuum slope. The arrow shows the direction of the increasing alteration of meteorites offset from the Elenovka data in Moroz et al. (1996) and consistent with a trend from bright to dark materials on Eros; e) Band I depth versus Band I continuum slope with the dashed line outlining the general region of S-asteroids, the solid thin line indicating the approximate location of the ordinary chondrite meteorites (Fanale et al. 1992), and the connected boxes showing the alteration series of Moroz et al. (1996) from unaltered in the lower right, to partly altered, to altered inside the S-asteroid field. Dark Eros data lie in the more altered direction of the Moroz et al. (1996) progression and within the S-asteroid field; f) NIS reflectance at 902.7 nm versus Band I depth, again shown paralleling the Moroz et al. (1996) alteration trend; g) Band I center versus NIS reflectance at 902.7 nm shows weak correlation between reflectance and band center. The Elenovka trend is also shown.

influence of phase angle on wavelength dependent spectral contrast (Gradie and Veverka 1986).

A comparison of Band I and Band II continuum slopes is shown in Fig. 7c. The data cloud hints at a correlation between slopes. The brightness subsets emphasize this correlation with shallower slopes for brighter materials. Darker materials with steeper slopes appear spectrally more "red." This observation is consistent with Bell et al. (2002) LPF data. Figs. 7d and 7e show the Band I continuum slope has some correlation with both albedo and Band I depth. The NIS+ data cloud in Fig. 7d indicates a slight shallowing of the continuum slope with increasing albedo, and the brightness subsets emphasize the trend. In Fig. 7e, deeper band depth correlates with shallower slopes, a trend largely hidden in the full data set but apparent in the brightness subsets. The comparison of albedo to Band I depth in Fig. 7f shows the increase in band depth with albedo insinuated by Figs. 7d and 7e and agrees with MSI albedo versus color ratio trends in Murchie et al. (2002a). Finally, albedo compared with Band I center in Fig. 7g hints at a possible correlation with brighter materials having shorter wavelength band centers.

Regional Spectral Variations

To investigate regional or geologic relationships to the spectral variation seen in NIS+, we separate subsets of the data set for independent analysis. The geographic/morphologic subsets of NIS+ are shown in Fig. 5 and Table 6, and the derived parameters are listed in Table 7. We examine four main locations: Psyche crater, Himeros, Eros' equator, and the 2 ends or noses of the asteroid. Two subsets are extracted from Psyche: Central Psyche (CP)—the dark floor materials of Psyche crater, and Psyche rim (PR)—bright materials on the rim and walls of the crater. Himeros is also divided into the darker central Himeros (CH) and brighter Himeros rim (HR). The equator (EQ) is the ±10° latitude band around Eros excluding Psyche and Himeros; and the "noses" of Eros (NS) are the regions around 0° and 180° longitude that constitute the narrow ends of its oblong shape. Correlation plots of the geographic regions in Fig. 8 are centered on the parameters of the average NIS+ spectrum. The rim materials (PR and HR) are similar to bright Eros with relaxed reflectance criteria, but restricted location. Central materials (CP and CH) are geographic subsets of dark Eros with stricter (and darker) reflectance criteria (Tables 6 and 7).

Figure 8a shows Band I versus Band II center correlation. Central materials show longer wavelength Band I centers than other materials. The band depth correlation plot in Fig. 8b shows a similar separation of central materials with shallower Band I depth, with rim materials trending toward deeper Band I. In both Figs. 8a and 8b, Band II parameters are still relatively imprecise, even with the increased SNR of the averaged spectrum.

Figure 8c, comparing continuum slopes, shows region-dependent variation, and better Band I versus Band II correlation. Central Psyche, central Himeros, and the noses have steeper, redder slopes over both bands, while the rim materials trend toward shallower slopes. NIS albedo at 902.7 nm is compared with the Band I continuum slope in Fig. 8d. The Psyche and Himeros rim and wall materials are among the brightest on Eros, while central Psyche and Himeros are among the darkest. Linear trends from bright rim materials to dark central materials are also visible in Fig. 8e (Band I depth versus Band I slope), Fig. 8f (reflectance versus Band I depth), and Fig. 8g (reflectance versus Band I center). While the equatorial and nose regions plot toward the middle of the field (closer to the average Eros values), the noses are slightly darker and resemble central materials more closely than the equator. Substituting MSI reflectance at 754 or 951 nm for NIS reflectance shows the same trends with less variation in reflectance values. Figs. 9a–9c show correlation plots analogous to Figs. 8d, 8f, and 8g substituting MSI reflectance (754 nm) for NIS.

INTERPRETATIONS AND DISCUSSION

Mineralogy of Eros: Band Parameters

Figure 10 is a plot of BAR versus Band I center for the NIS+ data set overlaid onto a portion of the similar Gaffey et al. (1993) plot, which shows the expected fields of S(IV) asteroids (defined by the observed range of ordinary chondrite spectral parameters) and the estimated areas of chondrite classes from laboratory measurements in Gaffey and Gilbert (1998). The S(III) field falls on either side of the S(IV) space. The Eros telescopic average spectrum from Murchie and Pieters (1996) is shown for comparison. On the whole, the NIS+ data set maintains the impression (as in Veverka et al. [2000] and Bell et al. [2002]) of Eros as spectrally homogeneous within the noise of the data. The spread of NIS+ data fall within the S(IV) to "inner" or high-BAR S(III) fields of the Gaffey et al. (1993) S-asteroid classifications, while the mean of the cloud of individual NIS+ spectral parameters, plot almost on top of the telescopic average inside the S(IV) field. The parameters of the NIS+ average spectrum plot close to the olivine-pyroxene mixing line of Cloutis et al. (1986). As shown in Figs. 7a and 7b, the average spectrum with increased SNR display a shorter wavelength Band I center and a shallower Band II depth. The latter translates to a smaller Band II area relative to Band I and, thus, a lower BAR.

The cloud of the full data set spreads through the LL and L ordinary chondrite ranges as defined by Gaffey et al. (1993) and Gaffey and Gilbert (1998). The mean of the data cloud lies in the LL/L fields, while the average spectrum is within the more chemically reduced L chondrite field.

Spectral variations on Eros are highlighted in Fig. 11, which plots BAR versus Band I center for the brightness subsets
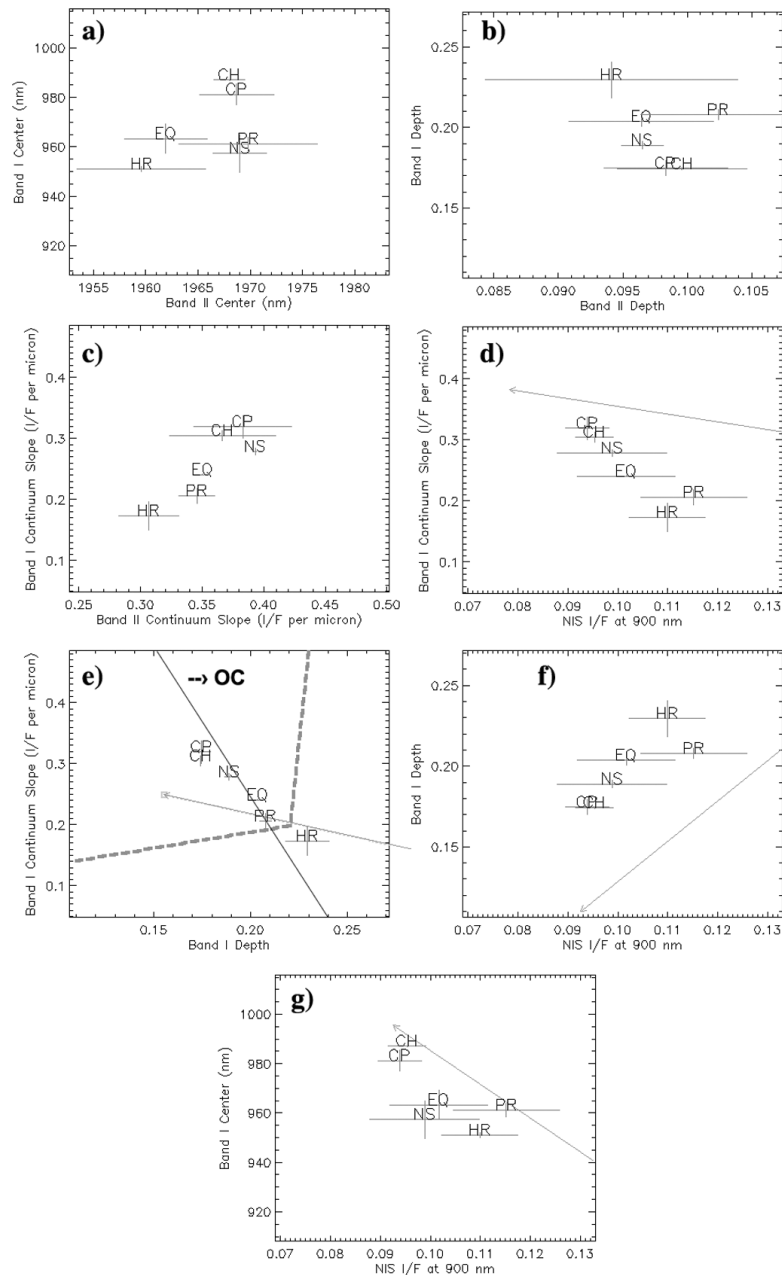
Fig. 8. Band parameter correlation plots for geographic/morphologic subsets of NIS+. The plots are in the same order as Fig. 7, but "zoomed in" to smaller scale ranges. CP = Central Psyche, CH = Central Himeros, PR = Psyche rim, HR = Himeros rim, EQ = Equator, NS = Noses. Parameter values are derived from the average spectrum of each subset, shown in Table 7: a) Band II center versus Band I center shows that the central materials of Psyche and Himeros have longer wavelength Band I centers. Even with the improved SNR of the average spectra, Band II parameters are still noisier than Band I; b) Band II depth versus Band I depth shows rim materials have deeper Band I depths, while central materials have shallower depths; c) Band I continuum slope versus Band II continuum slope shows a trend of steepening slope from rim materials to "central" materials. The equatorial region is intermediate, while the noses are slightly steeper sloped; d) NIS reflectance at 902.7 nm versus Band I continuum slope shows darker materials have steeper (redder) slopes. The arrow shows the direction of increasing alteration of meteorites, offset from the Elenovka data in Moroz et al. (1996) and consistent with a trend from rim materials to central materials, though with a different slope. This trend resembles the reflectance versus color ratio relationship in Murchie et al. (2002a), with reversed slope due to the inverse relationship of Band I depth with color ratio; e) Band I depth versus Band I continuum slope. Most subsets fall inside the S-asteroid field, where central materials lie in Elenovka's more altered direction. Rim materials lie in the less altered direction; f) NIS reflectance at 902.7 nm versus Band I depth, again shown paralleling the Elenovka alteration trend from rim to central materials; g) Band I center versus NIS reflectance at 902.7 nm shows higher correlation between low reflectance and long wavelength Band I center than Fig. 7g due to separation of more uniform central materials from the more inclusive dark Eros data set. The Elenovka trend is shown pointing from rim materials at the less altered end to central materials at the more altered end.
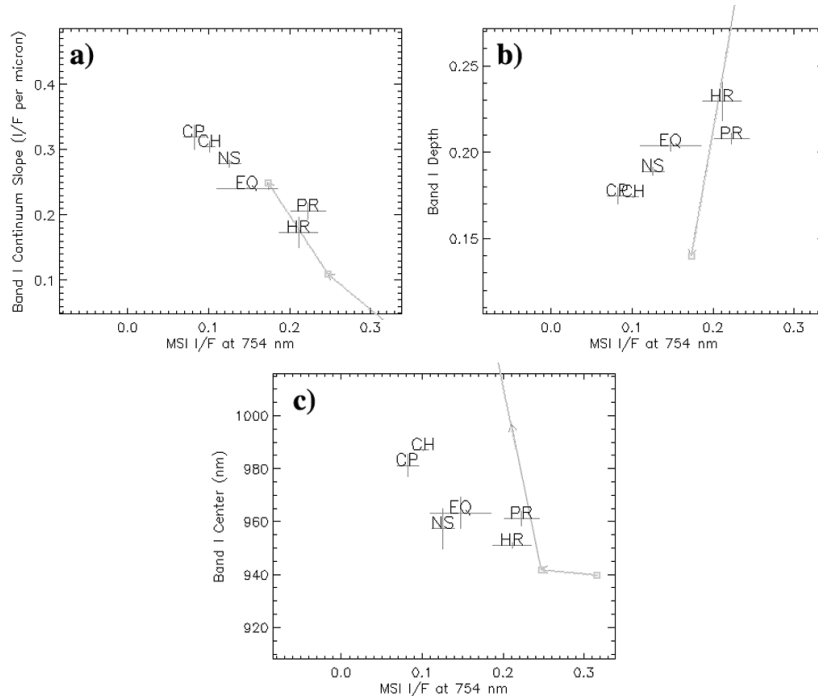
Fig. 9. Parts a–c of this plot correspond to Figs. 8d, 8f, and 8g, respectively, replacing NIS 902.7 nm reflectance with MSI 754 nm reflectance values. The parameter correlations are essentially the same as with NIS. As brightness decreases, near-IR slope increases, Band depth decreases, and Band I center goes to longer wavelengths. Reflectance values for MSI are less variable on an absolute scale. Elenovka experimental alteration data from Moroz et al. (1996) are plotted without scaling and show the same correlation of increasing alteration with bright to dark progression as with NIS: a) the Elenovka progression goes from unaltered (off the plot), to partially altered, to altered, closely paralleling the trend from rim to central materials; b) the partially altered to altered Elenovka path is similar to the Eros bright to dark material trend; c) Band I center goes to 1051 nm (off the plot) for the altered Elenovka sample.
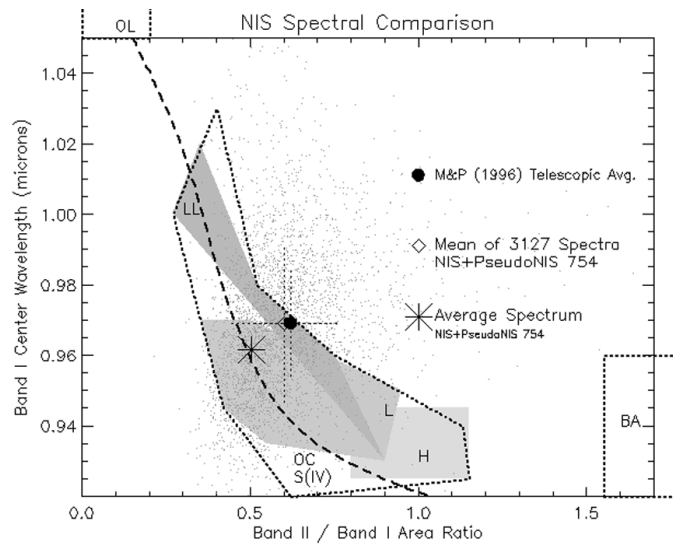

Fig. 10. Band area ratio (BAR) versus Band I center wavelength for the NIS+ data set, including parameters for each of the 3127 spectra in NIS+ (cloud of data points), the mean of parameters (diamond), and the average NIS+ spectrum (asterisk). We plot the parameters over the asteroid fields defined by Gaffey et al. (1993) and the ordinary chondrite meteorite fields from Gaffey and Gilbert (1998) and after McCoy et al. (2000). The S(III) asteroid field lies to either side of the S(IV) field in the higher and lower BAR directions. The telescopic average data (solid circle) is from Murchie and Pieters (1996). The meteorite fields shown are for olivine rich meteorites (OL), pyroxene-rich basaltic achondrites, and ordinary chondrites (OC). The OC field is subdivided into H, L, and LL chondrites (the fields of which overlap). The dashed line shows the olivine pyroxene mixing line of Cloutis et al. (1986). The error bars are 1σ uncertainty for each parameter for each data point in the cloud. The average spectrum's error bars are on the order of the symbol size.
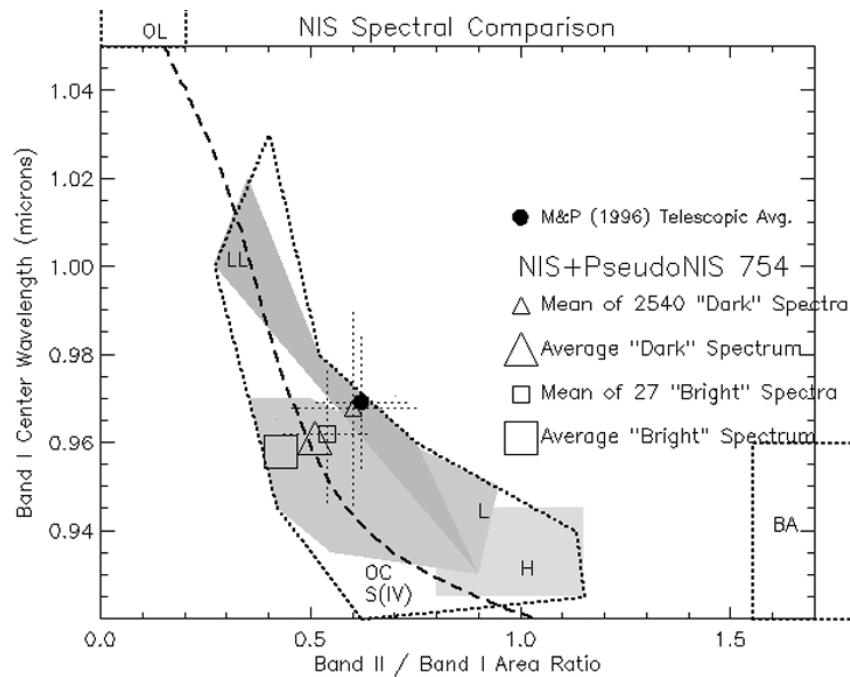
Fig. 11. BAR versus Band I center wavelength for NIS+ brightness subsets (see Tables 4, 5, and 7 for subset definitions parameter values). Progression from bright to dark materials suggests an alteration trend of increasing BAR and longer wavelength Band I center.

of NIS+. While the means (i.e., the mean parameters of the individual points in each data cloud) plot within 1σ of each other, the parameters of the average spectrum (determined in the same way as the "average Eros" spectrum in Fig. 3.) of each subset show significant separation (i.e., greater than their respective error bars) in the parameter space. Dark Eros materials plot almost at the same places as the full data set (for both mean of the cloud and the subset average) because the dark Eros is basically similar to average Eros. Bright materials have lower BAR values and shorter Band I centers. The direction of variation is nearly orthogonal to the olivine mixing line. Dark materials fall within the L/LL meteorite fields, while Bright materials plot within the observed L field and within the S(IV) ordinary chondrite envelope.

Spectral variations of the regional subsets are plotted in Fig. 12. Central Psyche and central Himeros plot just outside the S(IV) field in the longer BAR and longer wavelength Band I center direction on the edge of the high-BAR S(III) field (Gaffey et al. 1993). The other regions' parameters all fall within S(IV). The variation between rim and central materials is near orthogonal to the olivine-orthopyroxene mixing trend. Both the nose and equatorial regions plot on the mixing line, with nose materials plotting as less olivine-rich than the equator. Equatorial, nose, and rim regions plot inside the L chondrite field, while the central subsets plot outside all the chondritic meteorite fields. As with the S(III) asteroids 15 Eunomia, 43 Ariadne, and 532 Herculina (Gaffey et al. 1993), the long wavelength edge of Band II in the NIS+ data set may lie beyond the long wavelength limit of the NIS instrument, resulting in lower BAR values of NIS+ data.

Space Weathering

The albedo-discriminated subsets of the NIS+ data set can be directly compared to similar subsets examined in Clark et al. (2001). In that study, near-contemporaneous spectra of dark and bright materials on the Psyche rim and wall show a distinctive difference in reflectance, and their ratios show structure in both short (Band I region) and long (Band II region) wavelengths (Figs. 12 and 14 in Clark et al. [2001]). Comparisons of the bright and dark NIS+ subsets are shown in Fig. 13. The bright rim/wall and dark central regions in Psyche (subsets PR and CP) and Himeros (HR and CH) are also shown. Figure 13a shows the magnitudes of the reflectance differences between dark and bright materials on Eros. Bright Eros and central Psyche represent the most extreme difference in reflectance of the subsets under study.

NIS+ bright/dark ratios (Fig. 13b) show a downturn in the shorter wavelengths (and resulting broadening of Band I in dark materials) similar to that observed in Clark et al. (2001). The short wavelength downturn continues beyond the NIS wavelength range into the 754 nm-derived pseudo channel. Figure 13b shows the lowest contrast in Himeros (CH/HR in red) with a ratio around 0.87 between 1 and 2 microns. Bright/ dark Eros (black diamonds) and Psyche (CP/PR in blue) have similar ratios around 0.83, while the most extreme reflectance variations on Eros (CP/bright Eros in green) have a ratio around 0.80. All NIS+ ratios exhibit a slightly higher ratio in the Band I region—a slight band-broadening effect that shows as a hump around 1 micron. This feature may be present but is not prominent in Clark et al. (2001).
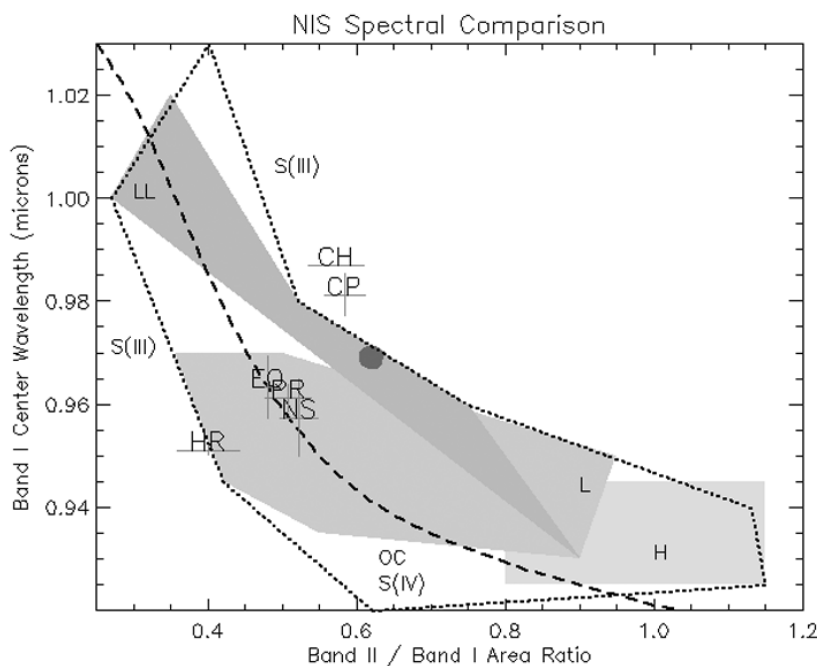
Fig. 12. BAR versus Band I center wavelength for NIS+ geographic/morphologic subsets (see Tables 6 and 7 for region definitions and parameter values). The plot range is narrower than Figs. 10 and 11 to focus on the S(IV) region. The S(III) regions to either side of S(IV) are also shown. The telescopic average (Murchie and Pieters 1996) is plotted as a grey circle. Bright rim/wall materials have shorter BAR and shorter wavelength Band I centers than the dark central materials of Psyche and Himeros, possibly describing a trend of increasing weathering. The variation between the most pristine-appearing materials (HR and PR) and the most weathered-looking (CH and CP) follows a trend, consistent with space weathering, orthogonal to the olivine mixing line, crossing from the low-BAR side of the S(IV) envelope into the high-BAR S(III) field. Nose and equatorial materials (and Psyche rim materials) plot along the olivine mixing line, with the noses plotting slightly more olivine-poor.

Clark et al. (2001) explored a variety of plausible causes for the dark/bright ratio, including mixing models designed to follow the alteration effects of "space weathering." In this context, space weathering is defined as alteration of the asteroidal "bedrock" material, probably caused by micrometeorite and ion bombardment of silicate minerals producing free metallic iron coatings on grains of regolith, resulting in spectral darkening, shallowing of the mafic silicate absorption bands, and reddening of the continuum slope. This hypothesis is discussed, modeled, and experimentally investigated in Pieters et al. (2000) and Hapke (2001). The reduced redness of the scatter-corrected NIS spectrum in long wavelengths provides an improved match to the mixing models for both bright and dark Eros materials presented in Fig. 17 of Clark et al. (2001). Likewise, the reduction in longest wavelength reflectance and the slight increase in reflectance from 1700 to 2000 nm provide for a closer match to the "Manbhoom + 5% dark component" assemblage in Bell et al. (2002). The NIS+ data set is consistent with both Clark et al.'s (2001) modeling of composition and optical maturity variations and with Bell et al.'s (2002) nonlinear mixing models.

Fig. 13b also shows reflectance ratios from laser-alteration experiments on the chondritic meteorite Elenovka by Moroz et al. (1996). In the experiments, an impulse laser treatment of powdered meteorite in a vacuum was used to simulate the effects of space weathering. The Elenovka experiments took the unaltered meteorite through an intermediate "partially altered" state and then an "altered" state with substantial melting and glass formation. The partially altered/unaltered ratio for Elenovka shown in Fig. 13b as a dotted line is similar to the NIS+ bright/dark ratio, though slightly more red-sloped and with a slightly lower ratio in Band I. Elenovka's altered/partially altered ratio shows a strong downturn shortward of 950 nm and higher values in the Band I and Band II regions (a substantial band-broadening effect). Band I variations in the NIS+ dark/bright ratios are more slight and less narrow in wavelength range, and the Band II effects are subtle if present at all. Figure 13b shows both Eros and Elenovka darkening with increased alteration. The Elenovka data implies that weathering from an unaltered material to a slightly altered material involves substantial darkening and some reddening. Progress from a slightly altered material to a more altered state involves more darkening and has a more pronounced effect on absorption bands (decreased band depth, increased slope and center wavelength, decreasing BAR). The full progression of Elenovka alteration shows a total reduction in reflectance of about 40%. This range is within both the MSI reflectance variation (Murchie et al. 2002) and the variation between the brightest and darkest individual NIS+ spectra.
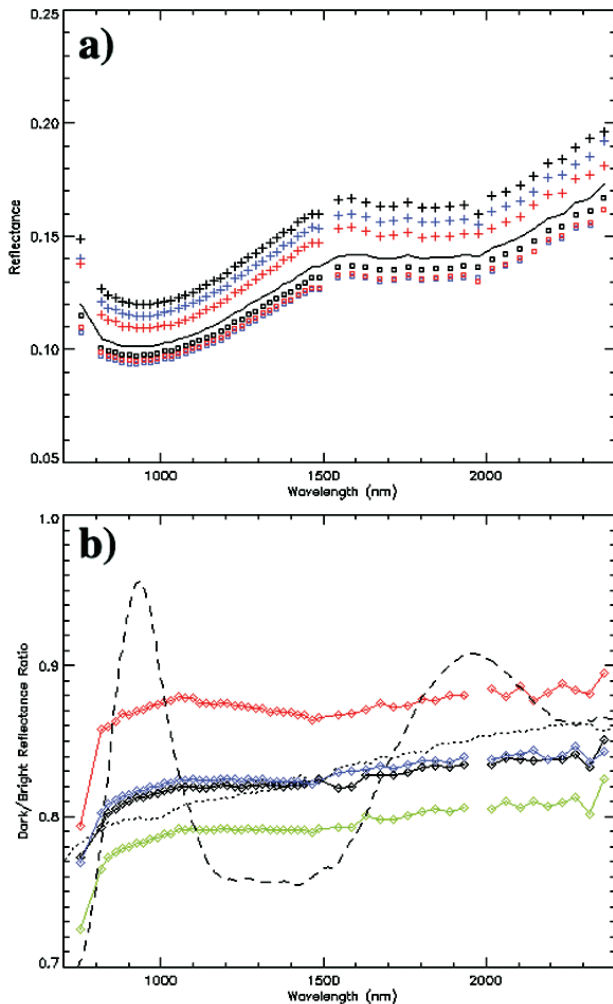
Fig. 13. These plots show spectra of dark and bright materials on Eros and brightness ratios for Eros and the experimentally weathered meteorite Elenovka (Moroz et al. 1996): a) NIS+ spectra for average Eros (solid line), bright Eros (black crosses), and dark Eros (dark squares) subsets. Psyche materials PR and CP are shown as blue crosses and boxes, respectively, and Himeros materials HR and CH are red. Bright Eros is the brightest reflectance subset of NIS+, and CP is the darkest overall; b) dark/bright ratios for Eros and Elenovka. Black diamonds are dark/bright Eros ratio, blue are CP/PR, red are CH/HR, and green are CP/bright Eros. The dotted line is the partially altered/unaltered ratio for Elenovka, and the dashed line is the altered/partially altered ratio. The downturn at short wavelengths and red slope in Eros ratios is similar to Psyche bright/dark ratios of Clark et al. (2001), band-broadening in the 1 micron region is more prominent in NIS+ data. Eros ratios resemble the less-altered ratio of Elenovka. The red slope of Eros ratios is not as prominent as in Elenovka. Band broadening for Eros at 1 micron is intermediate between the alteration ratios of Elenovka.

Moroz et al. (1996) use Elenovka laser alteration as a model for space weathering processes. The NIS+ band parameter correlation plots in Figs. 7d–7g, 8d–8g, and 9 include the Elenovka experimental data for comparison with trends on Eros. Elenovka's darkening and steepening Band I

slope (offset in the correlation plots from Elenovka's significantly higher original reflectance) is in the same direction as the bright to dark Eros (Fig. 12d) and rim to central subset (Figs. 8d and 9a) trends. NIS Band I slopes all fall in the partially altered to altered range of Elenovka data.

The reflectance versus Band I depth trend from Moroz et al. (1996) in Figs. 7f, 8f, and 9b again shows similarities with the brighter to darker subset trends in NIS+. Table 7 shows the shift in Band I depth from bright to dark materials as on the order of 3–5%. The change in Elenovka's Band I depth going from unaltered to partially altered states is near zero and from partially altered to altered is on the order of 20%. The entire range of Eros Band I depths fall near the most altered end of Elenovka's induced weathering path. The magnitude of the change in Band I depth implies that the shift in Eros data, if due to similar weathering processes, is from a partially altered material to a more altered material.

Figures 7e and 8e include unscaled Elenovka band parameters along with NIS+ in the Band I depth versus Band I continuum correlation plots. The bright to dark and rim to central subsets lie close to the path of alteration of Elenovka. Brighter Eros materials lie between partially altered and altered Elenovka, and darker materials fall close to altered Elenovka values. As Elenovka reaches its most altered state, and as Eros darkens, the data move into the S-asteroid region described by Fanale et al. (1992).

Sasaki et al. (2001) note that the Elenovka laser alteration experiments were conducted with too-long laser pulse durations and that some spectral changes may be attributable primarily to glass formation. Their experiments on olivine samples with shorter duration pulses show similar darkening and reddening alteration effects. Olivines typically do not have Band II absorptions, so BAR changes are not included in their analysis. However, the work of Sasaki et al. (2001) does exhibit a steepening of near-IR slope, decrease in Band I depth, and increase in wavelength of Band I center with increasing alteration. The olivine experiments are consistent with Moroz et al.'s (1996) experimental alteration trends and the dark to bright material trends on Eros. Hapke's (2001) detailed weathering models and experiments applied to S-asteroid alteration also assert the darkening, reddening, and absorption band-subduing effects of space weathering. In all, the similarities between the alteration experiments, modeling of space weathering, and Eros dark/bright data suggest that some kind of space weathering process is responsible for most, if not all, of the variability of spectral parameters on Eros. The notable exception is the NIS+ BAR trend, which has a clear but opposite trend for bright-to-dark materials and crater rim/wall-to-floor materials compared to laboratory space weathering experiments, including Elenovka. This does not contraindicate space weathering but does suggest a process in addition to or other than both lunar-style space weathering (Lucey et al. 1998, 2000; Murchie et al. 2002a) and Ida-style weathering where significant spectral variations

are present but not accompanied by the large albedo differences seen on Eros (Chapman 1996).

Clark et al.'s (2001) results for Psyche, implying and modeling a space weathering connection between bright and dark materials, are supported by the NIS+ Psyche subsets (PR and CP). The Himeros rim/wall and central subsets (HR and CH), noted by Murchie et al. (2002a) and Robinson et al. (2002) as having similar brightness contrasts and spatial relationships to corresponding Psyche materials, are shown here to be spectrally consistent as well. Over the full NIS+ data set, brighter Eros materials appear "less altered" relative to the trends described by modeling and experimental weathering studies, while darker materials lie in the "more altered" direction. The addition of Himeros and other NIS+ findings support space weathering as a global surface process on Eros.

The implication that the floor of Psyche contains more space-weathered material has been discussed based on spectral properties (Clark et al. 2001), MSI color properties (Murchie et al. 2002a), and albedo, morphological and stratigraphic relationships (Robinson et al. 2002). Murchie et al. (2002a) link the weak color variations on Eros in Himeros and bright-walled craters with space weathering effects. Murchie et al. (2002a) and Robinson et al. (2002) show that steep slopes, predominantly the inner walls of craters, have the brightest materials and often show evidence of mass wasting down to darker floor materials. Based on spectral parameter variations with brightness and geographic/morphologic regions in the NIS+ data set, we agree with the findings and conclusions of the previous work and extend them beyond color differences with spectral analysis across Eros. Though the CH/HR brightness ratio in Himeros is higher than CP/PR in Psyche (i.e., has a lower brightness contrast), the floor versus rim/wall materials of Himeros exhibit some stronger band parameter contrasts than corresponding Psyche materials. This implies similar processes acting in both locations and, possibly, the presence of less altered/more pristine materials in the Himeros rim/wall than in Psyche.

Other causes for spectral variation and trends on Eros still bear further investigation. For example, Ueda et al. (2002) point out that grain size variation can complicate interpretation of spectral parameters (including BAR) and may contribute to departures from expected space weathering trends, especially if the weathering process also affects grain size distribution.

If the brightest areas on Eros do, in fact, represent the least weathered materials and, therefore, the "freshest" samples of Eros mineralogy, then a key result of this study, referring back to Figs. 11 and 12, is that Eros falls solidly in the S(IV) taxonomic classification field of asteroids and predominantly in the L-type ordinary chondrite range of meteorite analogues, toward the L6 thermal metamorphic grade (Gaffey 1976; McSween and Labotka 1993; Gaffey and Gilbert 1998). Average Eros materials fall in the same category, nearly atop the olivine mixing line (see Fig. B2 in the Appendix for a direct comparison of NIS+ average Eros to

an L6 "light" meteorite from Britt et al. [1992]), while the most weathered regolith layer, typified by the floor materials of Psyche and Himeros, is altered to a more LL chondrite (or S(IV)-to-S(III) asteroid) appearance.

Murchie et al. (2002a) note the less altered appearance of the equator in MSI color ratio data. In the NIS+ data set, the equatorial region as a whole exhibits average to slightly "fresher" appearance relative to average Eros and the rim/central subsets in Figs. 8 and 9. The EQ subset contains some bright crater wall materials but not in sufficient quantity (8 out of 224 spectra) to affect the average spectrum significantly (Table 7). Robinson et al. (2002) note that the equatorial belt of Eros experiences long periods of dawn/dusk (when either of the rotation poles are facing the sun). Concomitantly, when the spin axis of Eros is most perpendicular to the Eros-sun line, the equator is still not exposed to low-incidence sunlight for more than a few hours at a time. If the variation is not an artifact of Eros shape model errors affecting photometry, the equator's slightly less altered spectral signature may be the result of less exposure to solar-induced space weathering effects.

In mild contrast to the equator, the noses of Eros trend from average to slightly more weathered in appearance, and are otherwise not greatly distinguished from average Eros. Fig. 12 shows the average of the NS subset as possibly being less olivine-rich than other subsets, but the error bars make such a distinction tentative at best.

Olivine and Pyroxene Chemistry

Using McFadden et al.'s (2001) modification of the Cloutis et al. (1986) calibration of BAR for mixtures of orthopyroxene (opx) to olivine (olv), we analyze the opx/(opx + olv) ratio for the NIS+ data set and its subsets. The mean of 3127 NIS+ spectra, with BAR of 0.60 ± 0.16, gives an opx wt% of approximately $34 \pm 8\%$. The weight percent determinations are independent of absolute grain size but assume the grain sizes of opx and olv are similar. The NIS+ average spectrum, with BAR of 0.51 ± 0.02, narrows the wt% range to $31 \pm 2\%$. (Some comparisons from normative chemistry of chondritic meteorites by McSween et al. [1991] are: all $\pm$ approx 10%: H $\approx$ 43, L $\approx$ 35, LL $\approx$ 29.) The most divergent subsets of NIS+ in the BAR parameter are the Himeros rim subset (average spectrum BAR = 0.40 ± 0.04) and the Central Psyche subset (average spectrum BAR = 0.58 ± 0.03). The olivine wt% range, thus, varies at its most extreme from 24–35%. These values are significantly different from both McFadden et al. (2001) and Bell et al. (2002), likely due to the removal of scattered light effects on the BAR. However, the upper and lower bounds of the derived olivine ratio appear to have geologic significance: least olivine in the bright rim/wall materials of Himeros, Psyche, and other craters; and highest olivine in the central floor regions of Psyche and Himeros. This observation and

the chondrite compositions of less weathered-appearing assemblages on Eros are in opposition to recent laser irradiation experiments (Hioi and Sasaki 2001) and lunar weathering trends (Lucey et al. 1998, 2000).

If the bright rim/wall materials are indeed the least weathered, most pristine areas on Eros (Clark et al. 2001; Murchie et al. 2002a; Robinson et al. 2002; this study), then they probably reflect the interior bulk mineralogy of the asteroid more accurately than the asteroid average or any other spectral subset. Considering only the least weathered-appearing materials on the asteroid (the bright: Eros, and HR subsets), the olivine wt% range for Eros below the surface layer is 24–29%.

The olivine content analysis assumes little or no clinopyroxene (cpx) is present. From Cloutis et al. (1986) and Gaffey et al. (1993), addition of cpx causes deviation away from the olivine-orthopyroxene mixing line shown in Figs 10–12. McFadden et al. (2001) and McCoy et al. (2001) investigated the possibilities and implications of a two-pyroxene model for Eros. However, both stratigraphic (Murchie et al. 2002a; Robinson et al. 2002) and spectral (Clark et al. 2001; this study) relationships between bright-to-dark and wall-to-floor materials imply geological process explanations (i.e., mass wasting to expose fresh materials and space weathering of fresher materials to more altered appearance) rather than base compositional differences as the source for spectral variation on Eros. All significant variation in the NIS+ spectral parameters is explicable by space weathering of surface materials.

SUMMARY

In summary, we find:

1. Scattered light effects are identifiable and can be removed from NIS spectrometer data. Scatter corrected spectra have: (for both the 1 and 2 micron absorption bands) shallower infrared slopes; longer wavelength band centers; shallower band depths; and lower band area ratios.

2. A pseudo channel for NIS at 754 nm, derived from the MSI color ratio and co-location of NIS spectra and MSI north hemisphere, extends the effective spectral range of the NIS spectrometer to effectively complete coverage for the 1 micron absorption band.

3. 3127 high resolution, low noise spectra of the northern hemisphere of Eros with scattered light removal and appended 754 nm pseudo channel provide average spectral parameters for the asteroid. The data set can be further subdivided into brightness and geographically/morphologically discriminated subsets. NIS+ data requires no additional offsets or empirical corrections to be compared to other asteroids/meteorites.

4. NIS+ spectra remain more steeply red-sloped than telescopic observations of Eros. Other band parameters

are independent of continuum slope differences and do not affect comparison with other asteroid and meteorite data.

5. Brightness variations and ratios in earlier studies of Psyche crater and global color variations are verified and extended by the NIS+ data set. Geographically and geologically distinct areas on Eros show variation in brightness and other spectral parameters, but the asteroid as a whole shows no evidence for spectral/compositional heterogeneities that cannot be explained by space weathering.

6. Reflectance variations over the asteroid compared with laboratory alteration experiments, models of space weathering, and NEAR Multispectral Imager observations imply that the brightest materials on Eros (crater rims/walls) appear fresher and could be relatively less altered or unaltered, while the darkest materials (Psyche and Himeros floors) on Eros appear more weathered. However, comparison of other spectral parameters may imply that even the freshest exposed materials on Eros may be moderately to significantly space weathered.

7. Space weathering on Eros is apparently different from both lunar- and Ida-type weathering.

8. Composition models of Clark et al. (2001) and Bell et al. (2002) both look more favorable with NIS+ spectral data.

9. If the brightest materials on Eros are, in fact, representative of unweathered, pristine materials of a uniform body, then derived spectral parameters for Eros are consistent with an S(IV) asteroid with a low iron, thermally metamorphosed ordinary chondrite (L6 meteorite petrologic type) composition. The average surface materials, even if altered by space weathering, remain in the S(IV) and L6 classifications

10. The global average opx(opx + olv) for Eros is 0.31 ± 0.02 with variations for morphology and geography. The freshest-appearing materials on Eros—the rims/walls of Himeros and other craters—have a ratio ranging from 0.24–0.29 and may be more representative of "fresh" Eros beneath a weathered surface regolith layer.

we thank our reviewers for their efforts and input. This paper is dedicated to Montana.

REFERENCES

Adams J. B. 1974. Visible and near-infrared diffuse reflectance spectra of pyroxenes as applied to remote sensing of solid objects in the solar system. *Journal of Geophysical Research* 79:4829–4836.

Allen C. C., Morris R. V., Lauer H. V., Jr., and McKay D. S. 1993. Microscopic iron metal on glass and minerals: A tool for studying regolith maturity. *Icarus* 104:291–300.

Bell J. F., III, Izenberg N. I., Lucey P. G, Clark B. E., Peterson C., Gaffey M. J., Joseph J., Carcich B., Harch A., Bell M. E., Warren J., Martin P. D., McFadden L. A., Wellnitz D., Murchie S., Winter M., Veverka J., Thomas P., Robinson M. S., Malin M., and Cheng A. 2002. Near-IR reflectance spectroscopy of 433 Eros from the NIS instrument on the NEAR mission. I. Low phase angle observations. *Icarus* 155:119–144.

Britt D. T., Tholen D. J., Bell J. F., and Pieters C. M. 1992. Comparison of asteroid and meteorite spectra: Classification by principal components analysis. *Icarus* 99:153–166.

Chapman C. R. 1996. S-type asteroids, ordinary chondrites, and space weathering: The evidence from Galileo's fly-bys of Gaspra and Ida. *Meteoritics* 31:699–725.

Clark B. E. 1995. Spectral mixing models of S type asteroids. *Journal of Geophysical Research* 100:14443–14456.

Clark B. E., Lucey P. G., Helfenstein P., Bell J. F., III, Peterson C., Veverka J., McConnochie T., Robinson M. S., Bussey B., Murchie S. L., Izenberg N. I., and Chapman C. R. 2001. Space weathering on Eros: Constraints from albedo and spectral measurements of Psyche crater. *Meteoritics & Planetary Science* 36:1617–1637.

Clark B. E., Helfenstein P., Bell J. F., III, Peterson C., Veverka J., Izenberg N. R., Domingue D., Wellnitz D., and McFadden L. 2002. NEAR infrared spectrometer photometry of asteroid 433 Eros. *Icarus* 155:189–204.

Cloutis E. A. and Gaffey M. J. 1991. Pyroxene spectroscopy revisited: Spectral-compositional correlations and relationship to geothermometry. *Journal of Geophysical Research* 96:22809–22826.

Cloutis E. A., Gaffey M. J., Jackowski T. L., and Reed K. L. 1986. Calibration of phase abundance, composition, and particle size distribution for olivine-orthopyroxene mixtures from reflectance spectra. *Journal of Geophysical Research* 91:11641–11653.

Cloutis E. A., Gaffey M. J., Smith D. G. W., and Lambert R. St. J. 1990. Metal-silicate mixtures: Spectral properties and applications to asteroid taxonomy. *Journal of Geophysical Research* 95:8323–8338.

Fanale F. P., Clark B. E., and Bell J. F. 1992. A spectral analysis of ordinary chondrites, S-type asteroids, and their component minerals: Genetic implications. *Journal of Geophysical Research* 97:20863–20874.

Gaffey M. J. 1976. Spectral reflectance characteristics of the meoteorite classes. *Journal of Geophysical Research* 81:905–920.

Gaffey M. J., Bell J. F., Brown R. H., Burbine T. H., Piatek J., Reed K. L., and Chaky D. A. 1993. Mineralogic variations within the S-type asteroid class. *Icarus* 106:573–602.

Gaffey M. J. and Gilbert S. L. 1998. Asteroid 6 Hebe: The probable parent body of H-type ordinary chondrites and the IIE iron meteorites. *Meteoritics & Planetary Science* 33:1281–1295.

Gradie J. and Veverka J. 1986. The wavelength dependence of phase coefficients. *Icarus* 66:455–467.

Hapke B. 2001. Space weathering from Mercury to the asteroid belt. *Journal of Geophysical Research* 106:10039–10073.

Hapke B., Cassidy W., and Wells E. 1975. Effects of vapor-phase deposition processes on the optical, chemical, and magnetic properties of the lunar regolith. *The Moon* 13:339–353.

Hiroi T. and Sasaki S. 2001. Importance of space weathering simulation products in compositional modeling of asteroids: 349 Dembowska and 446 Aeternitas as examples. *Meteoritics & Planetary Science* 36:1587–1596.

Howser L. M. 2002. Measurement of brightness samples for CRISP sensor. Applied Physics Laboratory Memo A1F(2)02-U-086. 9 p.

Izenberg N. R., Bell J. F., Warren J. W., Murchie S. L., Peacock K., Darlington E. H., Carcich B., Chapman C., Clark B. E., Harch A., Heyler G., Joseph J., Martin P., McFadden L., Merline B., Robinson M., Veverka J., and Wellnitz D. 2000a. In-flight calibration of the Near Earth Asteroid Rendezvous mission's near infrared spectrometer, I. Initial calibrations. *Icarus* 148:550–571.

Izenberg N. R., Bell J. F., III, Clark B. E., Murchie S. L., Procketer L., Domingue D., Robinson S. M., McFadden L. K., Wellnitz D., Gaffey M. J., Lucey P., Chapman C., Veverka J., and the NEAR MSI/NIS Team 2000b. Investigation of visible color and near-IR spectra properties of Eros' surface using co-located NEAR NIS and MSI data. *Bulletin of the American Astronomical Society* 32:995.

Izenberg N. R., Bell J. F., III, Clark B. E., Murchie S. L., Gaffey M., Wellnitz D., McFadden L. A., and Robinson M. S. 2001. Comparison of color and spectral properties of Eros using NIS plus MSI (abstract #2083). 32nd Lunar and Planetary Science Conferencec. CD-ROM.

King T. V. V. and Ridley W. I. 1987. Relation of the spectroscopic reflectance of olivine to mineral chemistry and some remote sensing implications. *Journal of Geophysical Research* 92:11457–11469.

Lucey P. G., Blewitt D., and Hawke B. R. 1998. Mapping the FeO and TiO_2 content of the lunar surface with multispectral imagery. *Journal of Geophysical Research* 103:3679–3699.

Lucey P. G., Blewitt D., and Jollifff 2000. Lunar iron and titanium abundance algorithms based on final processing of Clementine ultraviolet-visible images. *Journal of Geophysical Research* 105:20297–202305.

McCoy T. J., Nittler L. R., Burbine T. H., Trombka J. I., Clark P. E., and Murphy M. E. 2000. Anatomy of a partially-differentiated asteroid: A "NEAR"-sighted view of acapulcoites and lodranites. *Icarus* 148:29–36.

McCoy T. J., Burbine T. H., McFadden L. A., Starr R. D., Gaffey M. J., Nittler L. R., Evans L. G., Izenberg N., Lucey P., Trombka J. I., Bell J. F., III, Clark B. E., Clark P. E., Squyres S. W., Chapman C. R., Boynton W. V., and Veverka J. 2001. The composition of 433 Eros: A mineralogical-chemical synthesis. *Meteoritics & Planetary Science* 36:1661–1672.

McFadden L. A., Wellnitz D. D. Shnaubelt M., Gaffey M. J., Bell J. F., III, Izenberg N. R., Murchie S. L., and Chapman C. R. 2001. Mineralogical interpretation of Eros from NEAR near-infrared spectrometer low phase flyby. *Meteoritics & Planetary Science* 36:1711–1726.

McSween H. Y., Jr., Bennett M. E., III, and Jarosewich E. 1991. The mineralogy of ordinary chondrites and implications for asteroid spectrophotometry. *Icarus* 90:107–116.

McSween H. Y., Jr. and Labotka T. C. 1993. Oxidation during metamorphism of the ordinary chondrites. *Geochimica et Cosmochimica Acta* 57:1105–1114.

Moroz L. V., Fisenko A. V., Semjonova L. F., Pieters C. M., and Korotaeva N. N. 1996. Optical effects of regolith processes on S-

asteroids as simulated by laser shots on ordinary chondrite and other mafic materials. *Icarus* 122:366–382.

Murchie S. L. and Pieters C. M. 1996. Spectral properties and rotational spectral heterogeneity of 433 Eros. *Journal of Geophysical Research* 101:2201–2214.

Murchie S. L., Robinson M., Hawkins S. E., Harch A., Helfenstein P., Thomas P., Peacock K., Owen W., Heyler G., Murphy P., Darlington E. H., Keeney A., Gold R., Clark B., Izenberg N., Bell J. F., Merline W., and Veverka J. 1999. Inflight calibration of the NEAR multispectral imager. *Icarus* 140:66–91.

Murchie S. L., Rovinson M., Clark B., Li H., Thomas P., Joseph J., Bussey B., Domingue D., Veverka J., Izenberg N., and Chapman C. 2002a. Color variations on Eros from NEAR multispectral imaging. *Icarus* 155:145–168.

Murchie S. L., Robinson M., Domingue D., Li H., Prockter L., Hawkins S. E., III, Owen W., Clark B., and Izenberg N. 2002b. Inflight calibration of the NEAR multispectral imager, II. Results from Eros approach and orbit. *Icarus* 155:229–243.

Pieters C., Taylor L., Noble S., Keller L., Hapke B., Morris R., Allen C., McKay D., and Wentworth S. 2000. Space weathering on airless bodies: Resolving a mystery with lunar samples. *Meteoritics & Planetary Science* 35:1101–1108.

Robinson M. S., Thomas P. C., Veverka J., Murchie S. L., and Wilcox B. B. 2002. The geology of 433 Eros. *Meteoritics & Planetary Science* 37:1651–1684.

Sasaki S., Nakamura N., Hamabe Y., Kurahashi E., and Hiroi T. 2001. Production of iron nanoparticles by laser irradiation in a simulation of lunar-like space weathering. *Nature* 410:555–557.

Thomas P. C., Joseph J., Carcich B., Veverka J., Clark B. E., Bell J. F., Byrd A. W., Chomko R., Robinson M., Murchie S., Prockter L., Cheng A., Izenberg N., Malin M., Chapman C., McFadden L. A., Kirk R., Gaffey M., and Lucey P. G. 2002. Eros: Shape, topography, and slope processes. *Icarus* 155:18–37.

Trombka J. I., Squyres S. W., Brückner J., Boynton W. V., Reedy R. C., McCoy T. J., Gorenstein P., Evans L. G., Arnold J. R., Starr R. D., Nittler L. R., Murphy M. E., Mikheeva I., McNutt R. L., McClanahan T. P., McCartney E., Goldstein J. O., Gold R. E., Floyd S. R., Clark P. E., Burbine T. H., Bhangoo J. S., Bailey S. H., and Petaev M. 2000. The elemental composition of asteroid 433 Eros: Results of the NEAR-Shoemaker X-ray spectrometer. *Science* 289:2101–2105.

Ueda Y., Hiroi T., Pieters C. M., and Miyamoto M. 2002. Changes of band I center and band II/band I area ratio in reflectance spectra of olivine-pyroxene mixtures due to the space weathering and grain size effects (abstract #2023). 33rd Lunar and Planetary Science Conference. CD-ROM.

Veverka J., Bell J. F., III, Thomas P., Harch A., Murchie S., Hawkins S. E., III. Warren J. W., Darlington H., Peacock K., Chapman C. R., McFadden L. A., Malin M. C., and Robinson M. S. 1997. An overview of the NEAR multispectral imager-near infrared spectrometer investigation. *Journal of Geophysical Research* 102:23709–23727.

Veverka J., Robinson M., Thomas P., Murchie S., Bell J. F., Izenberg N., Chapman C., Harch A., Bell M., Carcich B., Cheng A., Clark B., Domingue D., Dunham D., Farquhar R., Gaffey M. J., Hawkins E., Joseph J., Kirk R., Li H., Lucey P., Malin M., Martin P., McFadden L., Merline W. J., Miller J. K., Owen W. M., Peterson C., Prockter L., Warren J., Wellnitz D., Williams B. G., and Yeomans D. K. 2000. NEAR at Eros: Initial imaging and spectral results. *Science* 289:2088–2097.

Warren J. W., Peacock K., Darlington E. H., Murchie S. L., Oden S. F., Hayes J. R., Bell J. F., III, Krein S. J., and Mastandrea A. (1997) Near infrared spectrometer for the Near Earth Asteroid Rendezvous mission. *Space Science Reviews* 82:101–167.

APPENDIX A

This appendix illustrates the scattered light correction for NIS calibrated data derived from the high-resolution data set (phases M and N) photometrically corrected to incidence = 30° and emission = 0°. Figure A1 shows the 32 ×

32 matrices of relative response. Equations 1 and 2, using the relative response matrices, an average high-resolution Eros spectrum, and the ground radiance calibration spectrum produce a correction vector, which we smooth with a 5th order polynomial fit. Table A1 shows the resulting coefficients we use.
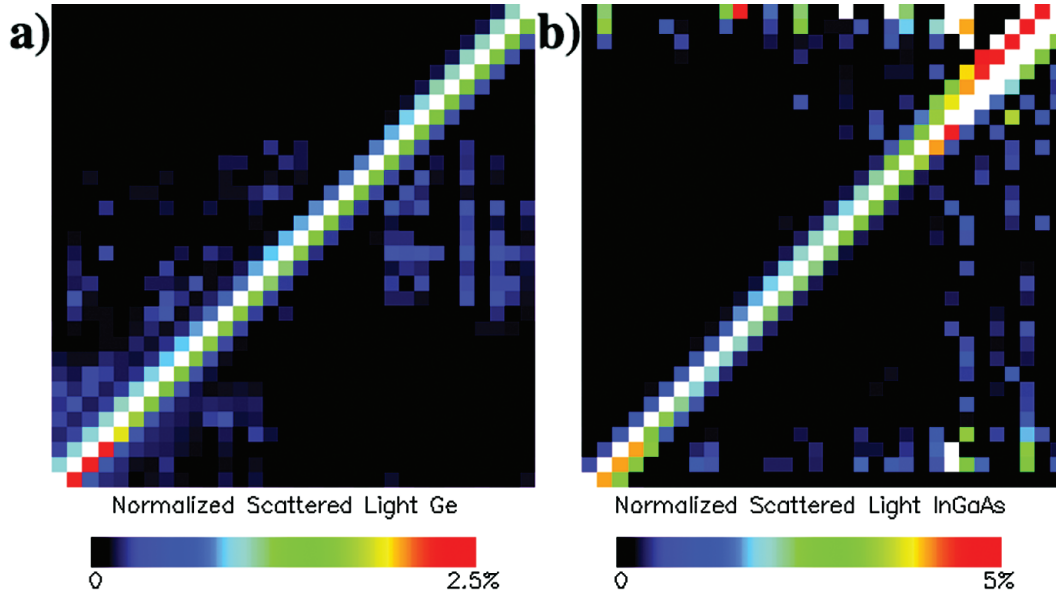

Fig. A1. Relative response matrices for the Ge and InGaAs detectors. The X-direction shows the 32 detectors of each of the 2 NIS detectors. The Y-direction (increasing upward) shows relative signal strength incoming to a given channel X from all wavelengths in the detector. At coordinates X = Y, where the incoming light wavelength equals the bandpass of the NIS channel, the relative response is 1.0. Nonzero values where X ≠ Y denote scattered light.

Table A1. Scattered light correction for the NIS+ data set. Multiply calibrated NIS data by these coefficients to remove scattered light effect from data.

#	Band Center (nm)	#	Band Center (nm)
1	0.9990	33	–
2	1.0024	34	–
3	1.0050	35	–
4	1.0070	36	–
5	1.0082	37	0.9970
6	1.0089	38	0.9989
7	1.0092	39	1.0008
8	1.0090	40	1.0026
9	1.0085	41	1.0042
10	1.0077	42	1.0053
11	1.0067	43	1.0059
12	1.0056	44	1.0058
13	1.0043	45	1.0049
14	1.0030	46	1.0031
15	1.0017	47	1.0005
16	1.0004	48	0.9969

Table A1. Scattered light correction for the NIS+ data set. Multiply calibrated NIS data by these coefficients to remove scattered light effect from data.

#	Band Center (nm)	#	Band Center (nm)
17	0.9991	49	0.9924
18	0.9979	50	0.9872
19	0.9968	51	0.9812
20	0.9957	52	0.9748
21	0.9949	53	0.9682
22	0.9941	54	0.9617
23	0.9935	55	0.9558
24	0.9931	56	0.9509
25	0.9928	57	0.9475
26	0.9927	58	0.9464
27	0.9927	59	0.9483
28	0.9929	60	0.9541
29	0.9932	61	–
30	0.9936	62	–
31	0.9942	63	–
32	0.9948	64	–

APPENDIX B

Sufficiency of NIS+ Extended Spectrum Band I Coverage

We compare the extended NIS spectrum to both the telescopic average from Murchie and Pieters (1996) and several chondritic meteorites from Britt et al. (1992). Figure B1 shows the different spectra under consideration, and Fig. B2 shows the BAR versus Band I center plot. The "short shoulder" of Band I is at or near 750 nm in the telescopic spectrum, so cutting up the spectrum shorter than that wavelength has no effect on the band parameters. The meteorite spectra short shoulders all extend below 750 nm, but, in each case, 754 nm lies past the inflection point of the absorption band curves. This implies that the remaining "incompleteness" of the band has little effect on band parameters. As shown in Fig. B2, the BAR of meteorite spectra cut off at 754 nm are ~0.01–0.02 higher than the full spectrum. Band I center of the cut off data is up to ~10 nm shorter. These effects lie primarily parallel to the olivine-orthopyroxene mixing line and may result in differences in $opx(opx + olv)$, with actual values on the order of 0.01–0.02 lower than those we derive. If the Eros spectrum is in fact similar to the telescopic average, then NIS+ spectral coverage is essentially complete and can be used at face value.

Cutoffs at longer wavelengths (Fig. B2) to equivalent of NIS channel 1 at 816 nm) induce over-estimation of both band area ratio and Band I center wavelength, as coverage of the 1 micron band becomes less and less complete.
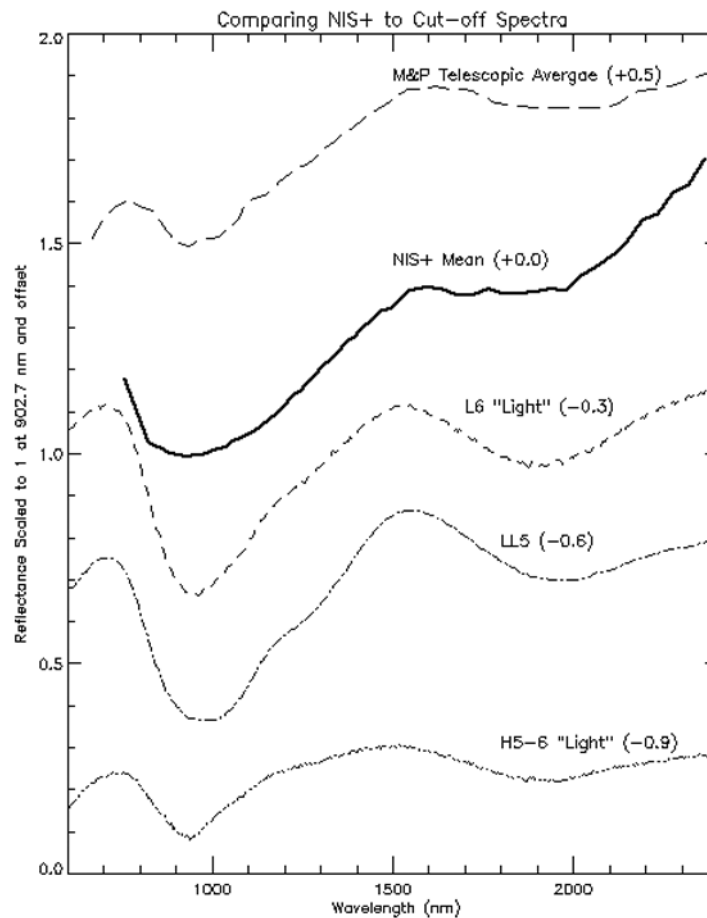

FIG. B1. Plot showing average Eros NIS+ spectrum, telescopic average (Murchie and Pieters 1996), and example L, LL, and H meteorites (Britt et al. 1992).
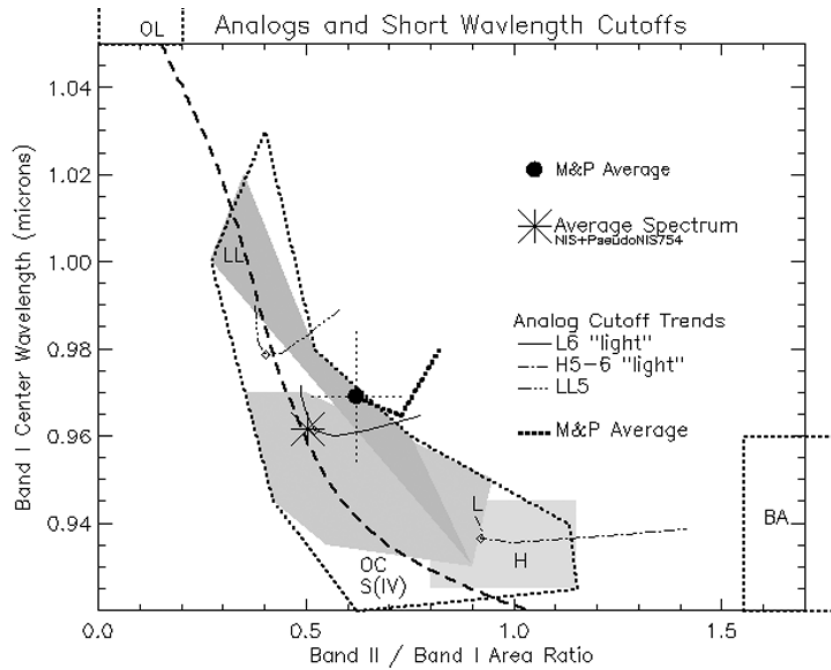
Fig. B2. BAR versus Band I Center plot (as in Figs. 15–17) showing telescopic and meteorite parameters, derived from the spectra shown in Fig. B1, cut off at increasing wavelengths, compared to average Eros from NIS+. The curves show the range from full Band I coverage (low BAR ends), to 754 nm cutoff (diamonds), to 816 nm cutoff (high BAR ends). The meteorite spectra with short wavelength shoulder of Band I cut off at progressively higher wavelengths exhibit a characteristic increase of band area ratio, and an initial decrease, then an increase in wavelength of the Band I center. The NIS+ average spectrum plots close to the L6 "light" chondrite spectrum cut off at 754 nm.